Simulation and Optimization of Second-Harmonic Generation with Incoherent Broadband Laser Pulses

Simulation und Optimierung von Frequenzverdopplung mit Inkohärenten Breitbandigen Laser Pulsen

Masterthesis by Marcus Malki

Date of submission: September 14, 2022

1. Review: Prof. Dr. Vincent Bagnoud

2. Review: Dr. Zsuzsanna Slattery-Major

Darmstadt



Physics Department Institute of Nuclear Physics AG Vincent Bagnoud Simulation and Optimization of Second-Harmonic Generation with Incoherent Broadband Laser Pulses

Simulation und Optimierung von Frequenzverdopplung mit Inkohärenten Breitbandigen Laser Pulsen

Master Thesis by Marcus Malki

Review: Prof. Dr. Vincent Bagnoud
 Review: Dr. Zsuzsanna Slattery-Major

Date: September 14, 2022

Darmstadt

Erklärung zur Abschlussarbeit gemäß § 22 Abs. 7 und § 23 Abs. 7 APB der TU Darmstadt

Hiermit versichere ich, Marcus Malki, die vorliegende Masterthesis ohne Hilfe Dritter und nur mit den angegebenen Quellen und Hilfsmitteln angefertigt zu haben. Alle Stellen, die Quellen entnommen wurden, sind als solche kenntlich gemacht worden. Diese Arbeit hat in gleicher oder ähnlicher Form noch keiner Prüfungsbehörde vorgelegen.

Mir ist bekannt, dass im Fall eines Plagiats (§ 38 Abs. 2 APB) ein Täuschungsversuch vorliegt, der dazu führt, dass die Arbeit mit 5,0 bewertet und damit ein Prüfungsversuch verbraucht wird. Abschlussarbeiten dürfen nur einmal wiederholt werden.

Bei der abgegebenen Thesis stimmen die schriftliche und die zur Archivierung eingereichte elektronische Fassung gemäß § 23 Abs. 7 APB überein.

Bei einer Thesis des Fachbereichs Architektur entspricht die eingereichte elektronische Fassung dem vorgestellten Modell und den vorgelegten Plänen.

Darmstadt, 14. September 2022

Marcus Malki

Contents

| 1 Introduction | | | | 8 | |
|----------------|------|----------|---|----|--|
| 2 | Fund | dament | als | 15 | |
| | 2.1 | Narrov | w Band Second-Harmonic Generation - The Baseline | 15 | |
| | | 2.1.1 | Mixing Equations | 15 | |
| | | 2.1.2 | | | |
| | | 2.1.3 | | | |
| | | 2.1.4 | Group Velocity Mismatch | | |
| | | 2.1.5 | Spatial Walk-Off | | |
| | | 2.1.6 | Sellmeier Equations | | |
| | 2.2 | Extens | sion to Broadband Second-Harmonic Generation | | |
| | | 2.2.1 | Mixing Equations | | |
| | | 2.2.2 | Dispersive Effects and Temporal Walkoff | | |
| | | 2.2.3 | Incoherent Laser Pulses | 29 | |
| 3 | Lase | er Syste | ems | 32 | |
| | 3.1 | The Pl | HELIX Laser | 33 | |
| | | 3.1.1 | Temporal and Spatial Parameters | 34 | |
| | | 3.1.2 | | | |
| 4 | SHG | Simula | ation Tools | 37 | |
| | 4.1 | Analyt | ical Solutions | 37 | |
| | | • | rical Tools | | |
| | | 4.2.1 | | | |
| | | 4.2.2 | Extension to Two-Dimensional Simulation | | |
| | | 4.2.3 | | | |
| | | | 4.2.3.1 SHG with Type II Phase Matching | | |
| | | | 4.2.3.2 Type I Phase Matching and Bandwidth Narrowing | | |
| | | | 4.2.3.3 Group Velocity Matched and Phase Matched SHG | | |
| | | | | | |

| Re | References 72 | | | | | |
|----|---------------|-----------------|--------------------|--|----------|--|
| 6 | Sumi | mary & | Outlook | | 70 | |
| 5 | 5.1 5.2 | Benchi Two-D | imension | on of the One-Dimensional Narrow Band Simulations al Simulations in Comparison to PHELIX Shots | 61 | |
| | | | 4.2.4.1 4.2.4.2 | 51 | 53 55 | |

1 Introduction

Thermonuclear fusion of deuterium and tritium promises to be a clean energy source [1] with the possibility to provide great amounts of energy [2]. For this, the deuterium and tritium need to be heated to a sufficiently high temperature around 15 keV to start the fusion process [3].

Several different ways to achieve fusion are being pursued like for example the Magnetic Confinement Fusion (MCF) [3] and Inertial Confinement Fusion (ICF) [4]. MCF, as the name already states, uses magnetic fields to confine the deuterium and tritium (D-T) which, at the needed temperatures, are in the form of a plasma. Heating can for example be achieved by inducing a current inside the plasma, that by Ohmic heating, increases the temperature. The MCF approach with Ohmic heating is for example used at the International Thermonuclear Experimental Reactor (ITER) [3].

ICF on the other hand works by compressing a pellet of deuterium and tritium and heating it, in order to start a fusion reaction. The density of the so-called hot-spot, where fusion initially occurs, needs to be sufficiently high for the alpha particles, that are formed in the fusion reaction, to deposit their energy inside the confined plasma, thereby further increasing the plasma temperature and enabling more fusion reactions to occur. This dynamic is called ignition and can be achieved at ion temperatures of $10\,\mathrm{keV}$ with an aerial density of $\rho R \geq 0.3\,\mathrm{g/\,cm^2}$ where ρ is the mass density and R the radius of the hot-spot [4].

The compression is achieved by heating the shell of the millimeter sized D-T pellet with high intensity laser pulses [5]. The shell is made of carbohydrates and turns into a plasma due to the laser pulse depositing its energy in the shell [4]. It then rapidly expands and in turn, due to conservation of momentum, compresses the D-T fuel to the needed densities [2]. In the so-called direct drive ICF the laser is directly incident on the pellet whereas in indirect drive the laser heats a high-Z material that surrounds the pellet [6]. The high-Z material then emits x-rays that in turn heat the pellet shell [7].

Indirect drive ICF is used at the National Ignition Facility (NIF) in Livermore [5] or the Laser Mégajoule (LMJ) facility in France [8], for example.

Using thermonuclear fusion as an energy source requires a reactor that is economically viable which means that a positive energy gain in the fusion reaction is needed [2]. This has proven to be a challenging task as the laser plasma interaction is subject to instabilities, so-called laser-plasma instabilities (LPI), reducing the efficiency of the energy transfer from the laser to the pellet shell [1,9].

In recent years an important milestone has been reached as the energy released by a fusion reaction at NIF was twice the peak kinetic energy of the imploding shell of the pellet [10]. The energy yield is, however, still several orders of magnitude below the total energy that is needed to achieve fusion [10]. In order to yield enough energy to achieve an overall positive gain of the system, the laser plasma coupling in particular needs to be improved upon [11] which we will discuss in the following.

At first, an efficient energy transfer from the laser to the pellet shell, which is turned into a plasma by the laser, is necessary for efficient thermonuclear fusion [11]. It has been found that the efficiency with which the laser energy is absorbed by the plasma significantly increases for shorter wavelengths below 530 nm and longer pulse durations above 2 ns [11, 12]. For Nd:glass lasers at 1053 nm wavelength, which are commonly used in ICF experiments [4, 5, 8], it is thus beneficial to use harmonic conversion. This is a non-linear optical process that takes place in specific crystals and creates waves of half [13], a third [14], a fourth [15] or a fifth [16] the fundamental wavelength. Of these we will be mainly concerned with the wavelength halving (or frequency doubling), the so-called Second-Harmonic Generation (SHG), for pulses with a duration in the order of nanoseconds.

As mentioned before, one of the challenges in ICF experiments is the occurrence of instabilities in the laser plasma interaction [1,9]. The Stimulated Raman and Brillouin Scattering (SRS and SBS), for example, are instabilities that cause part of the incident light from the laser to be back reflected thus reducing the efficiency of the energy transfer from the laser to the plasma [4,7]. SRS and SBS are parametric instabilities where an incident photon decays into a back reflected photon and an electron- or ion-wave, respectively [7]. In the so-called Two Plasmon Decay (TPD), a photon decays into two electron waves [4,17]. The electron waves created by SRS and TPD generate fast electrons, that preheat the pellet core before the pellet is compressed. An increased temperature of the pellet core increases the energy needed to compress it to the intended densities [17].

During the compression itself, another instability can arise, the so-called Rayleigh-Taylor Instability (RTI). It is a hydrodynamic instability, which arises at the interface between two fluids exerting pressure onto each other and amplifies any imperfection in this interface [18]. In ICF, RTI arises between the ablator and the pellet core and limits the maximum compression that can be achieved [19]. The instability is seeded by non-

uniformity in the spatial laser profile incident on the pellet shell [20].

Beam non-uniformity and RTI can be mitigated with the indirect drive ICF approach because the heated high-Z material surrounding the pellet generates an x-ray pulse that is more uniform than the incident laser pulse. The drawback is a lower energy coupling efficiency from the laser to the pellet since energy is lost to heating the surrounding material [6]. Direct drive ICF can achieve more efficient laser plasma energy coupling but is also more sensitive to non-uniformity of the laser pulse, and thus RTI, [5] since thermal smoothing is weaker than in indirect drive ICF [4].

Several developments have been made to control instabilities. The beam non-uniformity, which for example seeds RTI, is improved by beam smoothing techniques [17].

This can for example be done by sending the laser beam through a random phase plate. The phase plate splits the laser beam into multiple beamlets with a different phase each which, upon focusing the laser beam, create a speckle pattern. This speckle pattern has a variation in intensity that is on the scale of a focus created without the random phase plate. The lateral small scale of the intensity variation also generates intensity variation in the propagation direction. Since the beam propagates through a plasma as it is absorbed, the varying intensity in propagation direction smoothes the distribution of the absorbed energy at each point along the surface of the pellet [21]. Smoothing only occurs along the propagation direction because lateral smoothing from thermal effects is small for the short wavelengths that are used in order to achieve efficient energy absorption [22].

For cases of small propagation depths of the laser in the plasma, the smoothness can be further increased by temporally varying the speckle pattern. This can for example be achieved by reducing the coherence time of the laser to below the temporal delay between the beamlets. In this case, the so-called Induced Spatial Incoherence (ISI), a phase plate is utilized that generates equal temporal delays between neighboring beamlets. Measurements with this technique have shown a decrease in SRS by up to three orders of magnitude when reducing the coherence time from 2 ns to 2 ps [23].

Temporal variation of the speckle pattern could also be achieved with the so-called Smoothing by Spectral Dispersion (SSD). Here a broadband beam is spectrally dispersed before it is sent through a random phase plate. The beamlets created by the phase plate thus have different frequencies which causes their phase difference to vary over time. With the random phase delay between the frequency components caused by the phase plate, the laser beam produces a speckle pattern that varies over time [20].

Since instabilities like SRS, SBS or TPD are parametric instabilities that rely on coherent lasers [1], a widely pursued approach is to use broadband, and thus temporally less coherent [24], lasers to suppress the growth of these instabilities [1,25,26].

Numerical simulations have shown that increasing the bandwidth of a laser to $\Delta\omega/\omega\approx1\%$ can increase the threshold intensities, above which SRS and TPD occur, by a factor between 2 and 5 depending on the instability and wavelength of the laser [27].

In order to achieve suppression of instabilities and to increase the energy transfer efficiency from a laser pulse to the plasma, efforts have gone into frequency conversion of incoherent broadband laser pulses [25,28,29].

This is challenging since efficient frequency conversion requires the so-called phase matching condition to be fulfilled which relates the incidence angle of the pulse on the mixing crystal to its wavelength. The angle at which phase matching is achieved is also called the phase matching angle. In general, phase matching is not fulfilled for wavelengths other than the central wavelength which can, depending on the crystal thickness, lead to SHG bandwidths far below the $\sim 1\%$ needed to suppress laser plasma instabilities. Several ways to extend the bandwidth of the frequency conversion have thus been investigated.

Gao et al. [25] have theoretically investigated the collinear frequency conversion of incoherent broadband pulses. Collinear in this means that all laser pulses involved in the conversion process propagate in the same direction. They propose to use a 15% deuterium doped DKDP crystal, which has a bandwidth of $12\,\mathrm{nm}$ (1.1% at $1053\,\mathrm{nm}$), for efficient frequency doubling with a predicted conversion efficiency of up to 80%.

DKDP (Potassium Dideuterium Phosphate) is a crystal that is similar to KDP (Potassium Dihydrogen Phosphate) with the difference that some hydrogen atoms in the lattice are replaced with deuterium atoms. Varying amounts of deuterium can be specified by the deuterium doping or deuteration level.

In particular, a DKDP crystal with a deuteration level of 15% allows for a phase matching that is in the first order insensitive to the wavelength of the input laser pulse. This increases its acceptance bandwidth for frequency doubling.

The frequency doubling of incoherent broadband laser pulses was investigated with a small aperture 15% DKDP crystal and shows conversion efficiencies up to 70% with a loss in bandwidth from 1% in the fundamental pulse to 0.6% in the harmonic pulse. This measurement is planned to be repeated and verified with a large aperture crystal once it is delivered [25].

A different approach is chosen by Szabó *et al.* [30] in which the laser pulse is angularly dispersed before frequency conversion. In this way, the change in the phase matching angle with the wavelength can be compensated which increases the acceptance bandwidth of the frequency conversion process from 0.52 nm to 20 nm [30].

Another approach is pursued by Dorrer *et al.* [28] where an incoherent broadband pulse is mixed with a coherent narrowband pulse of twice the frequency. The resulting laser pulse

is an incoherent broadband pulse with three times the frequency of the original incoherent pulse. To achieve this, the broadband pulse is, like in the approach by Szabó *et al.*, angularly dispersed to compensate for the variation in the phase matching angle. Additionally, a small offset to the phase matching angle of the central frequency is introduced by which an even broader spectrum can be achieved with only slight losses to the conversion efficiency of the central wavelength. This is because the maximum conversion efficiency for the wavelengths around the pulses central wavelength is reached by detuning the phase matching angle in the same direction from the central wavelength's phase matching angle. With this scheme the bandwidth of frequency tripling can be extend from $0.35\,\mathrm{nm}$ to $28\,\mathrm{nm}$ [28].

The work on this thesis is done at the PHELIX laser facility. PHELIX is the Petawatt High Energy Laser for Heavy Ion Experiments located at GSI (Gesellschaft für SchwerIonenforschung) in Darmstadt. It will be a platform for future experiments concerning the interaction of an incoherent broadband laser pulse with a plasma. An extension of the PHELIX laser to be capable of generating these incoherent pulses is however still needed. The goal of this work is to develop a simulation tool that is capable of simulating incoherent broadband SHG which should in particular be able to simulate the second-harmonic conversion at the PHELIX laser facility.

The theoretical basis for calculating narrowband frequency conversion has been laid by Armstrong *et al.* [31] in 1962. Extensions to this theory in order to accommodate broadband laser pulses can be found in [32].

In this thesis I will lay the foundation to simulating SHG for incoherent broadband pulses. I start by developing a tool to simulate coherent monochromatic light and will extend this to also include broadband and incoherent pulses in the further proceedings of this thesis. The assumed setup for the simulations will be collinear SHG since that is also the setup at PHELIX for SHG. I will also solely focus on KDP and DKDP crystals since 70% deuterated DKDP crystals are implemented at PHELIX. These crystals are also the only type of crystal that can currently be grown large enough for the apertures needed for the PHELIX laser and high energy lasers that are used in ICF experiments [28].

I will start in **chapter 2** by outlining the physical foundations and notations needed for the simulation of the SHG, taking a look at the mixing equations that describe SHG and the most important parameters in these equations. It is followed in **chapter 3** by a short overview over laser systems that focus on the study of laser plasma interactions, including the PHELIX laser and its parameters as these represent the input parameters to the SHG simulations in this thesis. **Chapter 4** deals with the description of the solutions of the aforementioned mixing equations. This includes analytical solutions of the mixing

equations and a discussion of numerical ways to solve them. In particular I will examine the numerical solutions developed in this work and study their results. In **chapter 5** I will benchmark the here developed code against the results of the other mentioned solutions to the mixing equations as well as compare the code's results to the measured conversion efficiency at the PHELIX laser facility. Finally, in **chapter 6** I will summarize the work done in this thesis and shortly outline the work following this thesis concerning broadband SHG and laser plasma instabilities.

2 Fundamentals

Firstly, we want to take a look at the physics underlying the simulations in this thesis, namely the Second-Harmonic Generation (SHG). We will discuss the equations describing this process and take a closer look at important parameters in these.

The SHG is a second order nonlinear optical effect that occurs in a nonlinear crystal when a laser pulse propagates through it. Similar to other nonlinear optical effects, the second order nonlinear polarization $\vec{P}^{(\text{NL})} = \epsilon_0 \chi^{(2)} \vec{E}^2$ of the crystal, which is the nonlinear response of the crystal to the electromagnetic field of the laser, can cause an energy transfer between electromagnetic fields of different frequencies. The parameters here are the total electric field \vec{E} , the second order dielectric susceptibility tensor $\chi^{(2)}$ and the vacuum permittivity ϵ_0 [32].

In the case of SHG the transfer occurs between light waves of frequencies ω and 2ω where the first will be referred to as fundamental or input and the latter as frequency doubled or harmonic wave.

2.1 Narrow Band Second-Harmonic Generation - The Baseline

2.1.1 Mixing Equations

The derivation of the mixing equations for the SHG shall be shortly outlined here starting with the wave equation for a light wave in a medium with a finite nonlinear susceptibility [33]

$$\left(\Delta - \frac{n^2}{c^2} \frac{\partial^2}{\partial t^2}\right) \vec{E} = \mu_0 \frac{\partial^2}{\partial t^2} \vec{P}^{(NL)}$$
(2.1.1)

using the index of refraction n, the magnetic vacuum permeability μ_0 and the vacuum speed of light c. The next step is to insert the superposition of three electric fields

 $\vec{E} = \vec{E}_{\omega_1} + \vec{E}_{\omega_2} + \vec{E}_{\omega_3}$ of frequencies ω_j , j=1,2,3 into equation (2.1.1) [33]. This yields the general equation for all second order nonlinear optical effects, which in particular includes the SHG where the frequencies are chosen to satisfy $\omega_3 = \omega_1 + \omega_2$ with $\omega_1 = \omega_2$. The term representing SHG in the nonlinear equation has the form [32]

$$\vec{P}_{\text{SHG}}^{(\text{NL})} = \epsilon_0 \chi^{(2)} \vec{E}_1 \vec{E}_2.$$
 (2.1.2)

The next step is to make the ansatz

$$\vec{E}_j(\vec{r},t) = \vec{e}_j \tilde{E}_j(z) e^{i(k_{jz}z - \omega_j t)}$$
(2.1.3)

with the unit vectors \vec{e}_j , the complex field envelopes \tilde{E}_j , the wave numbers k_{jz} in the z-direction and the frequencies ω_j for j=1,2,3 [32]. The propagation direction is set to the z-axis with which the Laplace operator in equation (2.1.1) can be simplified to $\partial^2/\partial z^2$.

The slowly varying envelope approximation is used where the envelope is assumed to have a slow variation in the propagation direction or more specifically a small derivative with respect to z. The second derivative of the field envelope is thus smaller than the first derivative and can thus be neglected [32].

From this, three differential equations can be extracted by comparison of the coefficients of the temporal waves $e^{-i\omega_j t}$. These equations have the form [33]

$$\begin{split} \frac{\partial \tilde{E}_{3}}{\partial z} &= i \frac{\omega_{3} d_{\text{eff}}}{n_{3} c} \tilde{E}_{1} \tilde{E}_{2} e^{i\Delta k z} \\ \frac{\partial \tilde{E}_{1}}{\partial z} &= i \frac{\omega_{1} d_{\text{eff}}}{n_{1} c} \tilde{E}_{2}^{*} \tilde{E}_{3} e^{-i\Delta k z} \\ \frac{\partial \tilde{E}_{2}}{\partial z} &= i \frac{\omega_{2} d_{\text{eff}}}{n_{2} c} \tilde{E}_{1}^{*} \tilde{E}_{3} e^{-i\Delta k z}, \end{split}$$

$$(2.1.4)$$

where the effective nonlinearity $d_{\rm eff}$ and the phase mismatch Δk are introduced. These are defined as [32]

$$d_{\text{eff}} = \vec{e}_1(\mathbf{d}\vec{e}_3\vec{e}_2)$$
 and $\Delta k = k_3 - k_2 - k_1$ (2.1.5)

using the third order tensor $2\mathbf{d} = \chi^{(2)}$ and the notations $k_{1z} = k_1$, $k_{2z} = k_2$ and $k_{3z} = k_3$. For SHG it suffices to write only two equations if the waves E_1 and E_2 are the same wave [33]. We will, however, use three equations instead, since this allows the study of SHG setups with distinguishable waves, as can be the case in birefringent crystals. A

common use case is that the input wave is split into an extraordinary and an ordinary wave, which in general have different indices of refraction [33].

Using the mixing equations we want to take a quick look at the energy flow between the three waves. From the equation for intensity

$$I_j = \frac{1}{2}c\epsilon_0 n_j \left| \tilde{E}_j \right|^2 = \frac{1}{2}c\epsilon_0 n_j \tilde{E}_j \tilde{E}_j^*$$
(2.1.6)

we can derive the Manley-Rowe relation for the energy flow between waves:

$$\frac{\partial}{\partial z} \frac{I_1}{\omega_1} = \frac{\partial}{\partial z} \frac{I_2}{\omega_2} = -\frac{\partial}{\partial z} \frac{I_3}{\omega_3} = -\epsilon_0 \chi^{(2)} \operatorname{Im}(\tilde{E_1}^* \tilde{E_2}^* \tilde{E_3} e^{-i\Delta kz}). \tag{2.1.7}$$

Besides highlighting the pairwise conversion of photons from the fundamental waves to the harmonic wave [33] we can observe that, in the case of perfectly aligned phases of the three waves, the energy flow rate is proportional to the field amplitudes of all three waves. Energy flow is however always restricted when one or more of the waves have low intensity and thus field amplitude.

In the following we will use the term conversion strength for the energy flow rate between the waves to prevent ambiguity.

We can extend the equations (2.1.4) to also include linear absorption of the waves in the crystal by adding a linear term to each of the equations. They take the form [31]

$$\frac{\partial \tilde{E}_{3}}{\partial z} = i \frac{\omega_{3} d_{\text{eff}}}{n_{3} c} \tilde{E}_{1} \tilde{E}_{2} e^{i\Delta kz} - \frac{\alpha_{3}}{2} \tilde{E}_{3}$$

$$\frac{\partial \tilde{E}_{1}}{\partial z} = i \frac{\omega_{1} d_{\text{eff}}}{n_{1} c} \tilde{E}_{2}^{*} \tilde{E}_{3} e^{-i\Delta kz} - \frac{\alpha_{1}}{2} \tilde{E}_{1}$$

$$\frac{\partial \tilde{E}_{2}}{\partial z} = i \frac{\omega_{2} d_{\text{eff}}}{n_{2} c} \tilde{E}_{1}^{*} \tilde{E}_{3} e^{-i\Delta kz} - \frac{\alpha_{2}}{2} \tilde{E}_{2},$$
(2.1.8)

with the linear absorption coefficients α_j for the respective waves. An integration of the differential equations (2.1.8) without the mixing terms over the propagation distance z yields the solutions $\tilde{E}_j(z) = \tilde{E}_j(0)e^{-\alpha_j z/2}$. The factor 1/2 in the exponent vanishes if the intensity is calculated from this. This represents the typical formulation of linear absorption.

It of course also breaks the Manley-Rowe relation as now the change in every wave intensity is proportional to the intensity itself and is thus generally not equal to the other changes in intensity.

2.1.2 Nonlinear Susceptibility

We will now take a look at the properties of the nonlinear susceptibility which governs the strength of a nonlinear interaction. It is a $3 \times 3 \times 3$ tensor $\chi^{(2)} \cong \chi^{(2)}_{ijk}(\omega_1, \omega_2, \omega_3)$ that, for all combinations of $\pm \omega_m$ with m=1,2,3, has 324 components for all different second order mixing processes This number can however be reduced to 10 independent components using the following symmetries [34].

First, the nonlinear polarization \vec{P} (equation (2.1.2)) is a measurable and thus a real quantity. Second, the first two indices can be exchanged, since the indices of the corresponding waves are interchangeable. When using lossless or nearly lossless media all three indices are interchangeable. This is assumed to be true for this work. The nonlinear susceptibility, or more commonly the nonlinear tensor $\bf d$, is then denoted in a 3×6 matrix that is multiplied with a 6-dimensional vector depending on the polarization of the electric fields [34]

$$\mathbf{d}\vec{e}_{3}\vec{e}_{2} = \begin{pmatrix} d_{11} & d_{12} & d_{13} & d_{36} & d_{15} & d_{16} \\ d_{16} & d_{22} & d_{23} & d_{24} & d_{36} & d_{12} \\ d_{15} & d_{24} & d_{33} & d_{23} & d_{13} & d_{36} \end{pmatrix} \begin{pmatrix} e_{31}e_{21} \\ e_{32}e_{22} \\ e_{33}e_{23} \\ e_{32}e_{23} + e_{33}e_{22} \\ e_{31}e_{23} + e_{33}e_{21} \\ e_{31}e_{22} + e_{32}e_{21} \end{pmatrix}.$$
(2.1.9)

Taking the crystal symmetry group into account, more coefficients are dependent on each other or equal to zero [35].

As mentioned in the introduction we are mainly concerned with KDP and DKDP crystals as they are used at PHELIX and are the only crystals that can be grown large enough for the large apertures needed for ICF lasers. These crystals belong to the symmetry group $\overline{4}2m$ [36], for which only the coefficient d_{36} is non-zero [35].

Now, using the principal axes of the crystal as a coordinate system, with the z-axis being the optical axis, the vectors \vec{e}_j can be represented as polar vectors with the angle θ between the propagation direction and the optical axis of the crystal and the azimuthal angle ϕ between the propagation direction and the x-axis. Depending on whether the electric field is ordinarily (o, $\theta=0$) or extraordinarily (e, $\theta\neq0$) polarized, the vector \vec{e}_j takes the form [36]

$$\vec{e}_{j,o}(\phi,\theta) = \begin{pmatrix} -\sin\phi \\ \cos\phi \\ 0 \end{pmatrix} \text{ and } \vec{e}_{j,e}(\phi,\theta) = \begin{pmatrix} \cos\theta\cos\phi \\ \cos\theta\sin\phi \\ -\sin\theta \end{pmatrix}. \tag{2.1.10}$$

Depending on the polarization of the three waves involved in the frequency mixing process, equation (2.1.5) for d_{eff} can be evaluated using equations (2.1.9) and (2.1.10). For a crystal in the $\overline{4}2m$ symmetry group, like for example a DKDP crystal, and assuming collinear propagation of the laser beams, the effective nonlinearity computes to [35]

$$d_{\text{eff}} = \begin{cases} d_{36} \sin \theta \sin 2\phi & \text{type I} \\ d_{36} \sin 2\theta \cos 2\phi & \text{type II}, \end{cases}$$
 (2.1.11)

where type I and type II denote phase matching schemes with specific polarizations. Type I has the fundamental wave polarized ordinarily and the harmonic extraordinarily, whereas type II has one fundamental in ordinary polarization and the other fundamental as well as the harmonic wave in extraordinary polarization.

For the nonlinear matrix element d_{36} of KDP and DKDP the literature provides different values (see table 2.1).

The value of d_{36} for a KDP crystal ranges from 0.376 to 0.46 pm/V with more recent sources giving preference to 0.39 pm/V [37, 38]. An overview over the different published values is given in table 2.1 sorted from top to bottom by the year of publication.

The values given in papers published before 1972 [39,40] were converted from Gaussian units to SI units using the conversion factor [34,41,42]

$$\frac{4\pi}{c \cdot 10^{-4}} = 4.192 \cdot 10^{-4} \frac{\text{m/V}}{\text{cm/erg}^{1/2}}.$$
 (2.1.12)

These two oldest measurements (see table 2.1) differ by more than their respective uncertainty from the more recently measured value $0.39\,\mathrm{pm/V}$. An explanation is given by Eimerl [43] suggesting a possible systematic error due to the use of focused laser beams in older measurements. Their evaluation is more difficult as walk-off has a greater influence at the focus and the focal spot is more sensitive to beam non-uniformities and diffraction. Since the values measured since 1986 starting with [43] all lie around $0.39\,\mathrm{pm/V}$ and papers such as [37, 38] recommend this value as well, it will be assumed as correct disregarding the two deviating values described above.

For the DKDP crystal there are significantly fewer measurements. Most values used in the literature [38, 42–45] refer to the relative measurement in [46] giving d_{36} for DKDP as $0.92\,d_{36}$ (KDP). Using d_{36} (KDP)= $0.39\,\mathrm{pm/V}$ coincidences with the absolute measurements of d_{36} (DKDP) giving 0.367 [44] and $0.37\,\mathrm{pm/V}$ [38] within the error margin.

A difficulty is that some literature [42, 47] uses the 0.44 pm/V and 0.46 pm/V value for $d_{36}(\text{KDP})$ and thus obtains a value of 0.4 pm/V for $d_{36}(\text{DKDP})$. This value is utilized by the

SNLO software [47], a commonly used numerical tool to calculate nonlinear processes, but will be disregarded in this work following the above discussion. SNLO confirms this as it uses $d_{36}(\text{KDP}) = 0.39 \, \text{pm/V}$ for KDP itself.

An additional difficulty with the effective nonlinearity is that the literature [38, 44, 46] does not state the deuteration level of the DKDP crystals measured. A DKDP crystal of an arbitrary deuteration level might thus have a d_{36} differing from the three values presented above. A dependence of the effective nonlinearity on the deuteration level was not described in the surveyed literature.

For this work we will assume that the 70% deuterated DKDP crystals implemented at PHELIX have the same effective nonlinearity as the measured crystals at $d_{36}(\text{DKDP}) = 0.37 \, \text{pm/V}$.

| $d_{36}(\text{KDP})$ in pm/V | d_{36} (DKDP) in pm/V | source |
|------------------------------|-------------------------------------|--------|
| | $0.92 \pm 0.04 d_{36}(\text{KDP})$ | [46] |
| 0.46 ± 0.04 | | [39] |
| 0.44 ± 0.02 | | [40] |
| 0.39 | | [43] |
| 0.376 ± 0.005 | 0.367 ± 0.012 | [44] |
| 0.39 ± 0.02 | | [14] |
| 0.39 | | [15] |
| 0.39 | 0.37 | [38] |
| 0.39 ± 0.03 | | [48] |
| 0.398 | | [49] |

Table 2.1: List of measured d_{36} values found in the literature sorted chronologically from top to bottom.

2.1.3 Phase and Group Velocity Mismatch and the Index of Refraction

The phase mismatch Δk is the most important parameter in the SHG since it directly influences the maximum efficiency that can be achieved by an experimental setup [32]. Efficiency is simply the ratio of the output energy at the doubled frequency and the input energy at the fundamental frequency. The phase mismatch is a measure for the speed in which the harmonic wave gets out of phase with the polarization generated by the two fundamental waves and thus destructively interferes with itself (see figure 2.1.1). This is called back conversion. Maximum conversion efficiency is achieved for $\Delta k = 0$ where the phase relation between polarization and harmonic wave is constant [32]. This is called

perfect phase matching or just phase matching and corresponds to the case in which the frequency doubled wave and the nonlinear polarization have the same phase velocity and thus always constructively interfere.

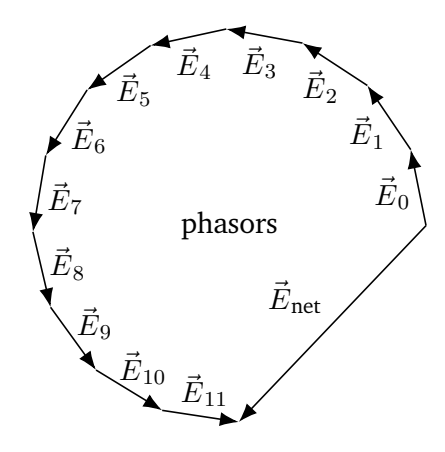


Figure 2.1.1: Phasors $\vec{E}_j = \vec{E} \exp(z_j \Delta k)$ at equidistant positions z_j accumulating a phase due to a phase mismatch Δk and thus resulting in destructive interference and a smaller net electric field amplitude of the harmonic wave. The phasors represent the complex field amplitude of the generated wave at different points along the propagation direction.

Because of the possibly vanishing conversion efficiency due to destructive interference, a lot of effort is put into minimizing the phase mismatch. For different crystals and wavelengths different phase matching techniques have been developed, for example the angular phase matching, the temperature phase matching and the quasi-phase-matching [33].

We will focus on the so-called type I and type II phase matching configurations defined above. These are angular phase matching techniques that are used with birefringent crystals. More specifically, these schemes operate with collinear input and output beams and have only one adjustable angle θ for phase matching, which is (equivalent to the angle θ defined in section 2.1.2) the angle between the \vec{k} -vectors and the optical axis of the crystal.

In order to better understand the phase matching schemes, let us take a look at the mathematical form of the phase mismatch. With the dependence of the wave number on the index of refraction it can be written as [36]

$$\Delta k = k_3 - k_2 - k_1 = \frac{n_3 \omega_3}{c} - \frac{n_2 \omega_2}{c} - \frac{n_1 \omega_1}{c} = \frac{\omega}{c} (2n_3 - n_2 - n_1)$$
 (2.1.13)

with the indices 1,2 representing the two fundamental waves and 3 representing the harmonic wave. In the case of SHG, the relation $\omega_3=2\omega_2=2\omega_1=:2\omega$ holds and perfect phase matching is achieved, if the difference $2n_3-n_2-n_1$ equals zero.

If we take three waves with the same polarization, two of which having the same wavelength, like in SHG, the phase matching condition will only be fulfilled for some special wavelengths for which the indices of refraction of the fundamental and harmonic waves coincide. In order to achieve phase matching for any wavelength, some way of changing the indices of refraction independently of each other is necessary.

The type I and II phase matching schemes therefore make use of both ordinary and extraordinary polarization in birefringent crystals, so that the angle dependence of the extraordinary index of refraction can be used to achieve phase matching.

As a reminder, in type I phase matching the two fundamental waves are set in ordinary polarization and the harmonic wave is in extraordinary polarization. Type II has one fundamental wave in ordinary and one in extraordinary polarization respectively and the harmonic wave in extraordinary.

When plotting the index of refraction over the angle θ (the angle between the propagation direction of the pulse and the optical axis of the crystal), perfect phase matching can, in the case of type I phase matching, be achieved at the point of intersection of the extraordinary ellipse and ordinary circle (see figure 2.1.2). In type II phase matching an intersection of the ellipses $2 \cdot n_{2\omega,e}(\theta)$ and $n_{\omega,e}(\theta) + n_{\omega,o}(\theta)$ is needed. If the two shapes do not intersect, perfect phase matching cannot be achieved.

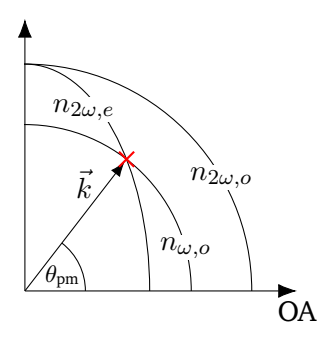


Figure 2.1.2: Scheme of the indices of refraction for type I phase matching depending on the angle between the \vec{k} -vector and the optical axis (OA). The phase matching condition is fulfilled at the intersection of the ellipse of $n_{2\omega,e}=n_3$ with the circle of $n_{\omega,o}=n_1=n_2$. Here, the phase mismatch vanishes and the wave vectors fulfill $\vec{k}_1=\vec{k}_2=2\vec{k}_3=\vec{k}$. The corresponding phase matching angle is denoted as $\theta_{\rm pm}$.

A phase mismatch of zero can in theory [33] lead to a conversion efficiency of one, but the highest efficiencies achieved in experiments are around 0.87 [16].

There are several factors limiting the maximum conversion efficiency in an experiment. The intensity distribution of a beam is never a perfect flat top, thus showing regions of low intensity. Since the change of the harmonic field amplitude in equation (2.1.4) is proportional to the electric field amplitude of the fundamental wave, these regions of lower intensity have an energy conversion at lower rates than regions of higher intensity. Because of this, the energy in the fundamental wave may not be fully converted to energy in the harmonic wave after the propagation through a finite crystal.

Additionally the phase matching may be imperfect leading to a nonzero phase mismatch. This can be caused by non planar wave fronts, for example, leading to deviations in k-vector angles and thus nonzero phase mismatch Δk [16]. This can significantly reduce the maximum achievable conversion efficiency down to zero as discussed at the beginning of section 2.1.3 [32].

Longer crystals may lead to better conversion of low intensity regions in the laser beam, but back conversion due to imperfect phase matching can occur at smaller phase mismatches and limit the total output energy in the harmonic wave [32].

2.1.4 Group Velocity Mismatch

As stated in the introduction, phase matching or near perfect phase matching with efficient frequency conversion is typically only fulfilled for a frequency band narrower than the $\sim 1\%$ bandwidth needed to suppress laser plasma instabilities. A way to achieve more broadband conversion efficiency is to set the second order term in the Taylor expansion of the phase mismatch to zero [25]:

$$\frac{\partial \Delta k}{\partial \omega} = \underbrace{\frac{2}{v_{g,3}} - \frac{1}{v_{g,2}} - \frac{1}{v_{g,1}}}_{=:\Delta v_g} \stackrel{!}{=} 0. \tag{2.1.14}$$

This is equivalent to the group velocity mismatch Δv_g being zero, where $v_{g,j}$ is the group velocity of the respective wave j=1,2,3. This condition is fulfilled in different crystals for only specific wavelengths, which are called retracing points. An example is a 15% deuterated DKDP crystal with type I phase matching where the group velocities of a $1053\,\mathrm{nm}$ ordinarily polarized and a $526.5\,\mathrm{nm}$ extraordinarily polarized wave are equal [25]. Other examples for retracing points include a wavelength of $1.5\,\mathrm{\mu m}$ for a BBO crystal [50] or $1.3\,\mathrm{\mu m}$ for an LBO crystal [51]. Group velocity matching can also be achieved with temperature phase matching [33] or the angular dispersion of the input laser pulse [29].

2.1.5 Spatial Walk-Off

Spatial walk-off is the result of a gradient of the refractive index over the propagation direction of a crystal. This causes the Poynting vector and the wave vector of the pulse to point in different directions [33]. This effect arises in anisotropic crystals, like for example in birefringent crystals for extraordinarily polarized beams. As an illustration we can again look at the ellipse of the extraordinary index of refraction in a birefringent crystal shown in figure 2.1.2. Depending on the angle of incidence θ , the index of refraction and thus the phase velocity of the wave varies. In the image of the Huygens-Fresnel principle this causes each wavelet to expand as an ellipsoid resulting in a Poynting vector not parallel to the wave vector and thus in an overall shift of the intensity distribution.

Due to spatial walk-off, a laser pulse's intensity distribution thus drifts perpendicular to the wave vector in the direction of the gradient of the refractive index. In birefringent crystals this direction lies in the plane spanned by the wave vector and the optical axis. The speed of the walk-off is determined by the angle between the wave and Poynting vector, which can be calculated based on the angle of incidence θ and the index of refraction of the crystal [33]

$$\tan\left(\theta_{\text{walk-off}}\right) = \frac{\left(\frac{n_0}{n_e} - 1\right)^2 \tan\theta}{1 + \left(\frac{n_0}{n_e} \tan\theta\right)^2}.$$
 (2.1.15)

In a 70% deuterated DKDP crystal we find walk-off angles between 1.25° and 1.5° , depending on the angle of incidence, for beams with the wavelengths 526.5 nm and 1053 nm. This results in an overall walk-off in the order of single millimeters for crystals with a length in the order of centimeters.

2.1.6 Sellmeier Equations

Since the phase mismatch and the group velocity mismatch and the walk-off are dependent on the indices of refraction, we want to take a look at their wavelength dependence. This is described by the so-called Sellmeier equations [52], which are empirical equations interpolating measurements at specific wavelengths [37, 53, 54]. For a different set of measurements this naturally leads to different Sellmeier equations for the same crystal. Specifically for KDP and DKDP crystals Lozhkarev *et al.* [37] examined the group velocity mismatch and fitted the Sellmeier equation to represent it correctly. Since group velocity mismatch is of interest for broadband SHG, we will make use of the Sellmeier equations given in [37] which have the following form:

$$n_{e}(\lambda) = \left(2.132668 + \frac{0.008637494}{\lambda^{2} - 0.012281043} + 3.2279924 \frac{\lambda^{2}}{\lambda^{2} - 400}\right) \left(1 - \frac{25}{24}D\right)$$

$$+ \left(2.126019 + \frac{0.008578409}{\lambda^{2} - 0.011991324} + 0.7844043 \frac{\lambda^{2}}{\lambda^{2} - 123.403407}\right) \cdot \frac{25}{24}D$$

$$n_{o}(\lambda) = \left(2.259276 + \frac{0.010089562}{\lambda^{2} - 0.012942625} + 13.00522 \frac{\lambda^{2}}{\lambda^{2} - 400}\right) \left(1 - \frac{25}{24}D\right)$$

$$+ \left(2.240921 + \frac{0.009676393}{\lambda^{2} - 0.015620153} + 2.2469564 \frac{\lambda^{2}}{\lambda^{2} - 126.920659}\right) \frac{25}{24}D$$

$$(2.1.165)$$

with the deuteration level D. The input wavelength λ is given in micrometers. These are, of course, the Sellmeier equations for both KDP and DKDP since KDP is just a DKDP with a deuteration D=0.

2.2 Extension to Broadband Second-Harmonic Generation

A spectrally coherent laser pulse has the property that all their spectral components have a fixed phase relation. With this property a broadband pulse can have a single short high intensity peak at points in time and space where all spectral components interfere constructively. An incoherent laser pulse on the other hand has a spectral phase that is random, especially no fixed phase relation can be found between two spectral components of the pulse. This has the effect that at no point, or rather very unlikely, all components interfere constructively and thus no single intensity peak emerges. The resulting temporal intensity profile is a temporal speckle with multiple intensity peaks.

In both cases this means that the approximation of a slowly varying amplitude of the laser pulse, i.e. a long pulse with a homogeneous intensity over the entire pulse duration, is no longer satisfied. We therefore need to revisit the mixing equations established for coherent narrow band laser pulses in section 2.1.1. We will this time approach the problem in the frequency domain.

Afterwards we will shortly investigate the dispersive effects that influence a broadband laser pulse as well as further discuss incoherence.

2.2.1 Mixing Equations

In broadband mixing there are multiple frequency components that all interact with each other. We therefore need a way to incorporate all possible frequency component interactions into the mixing equations. This can for example be achieved by integrating the mixing equation for all possible frequency combinations in the frequency domain [32]. The equations also incorporate the phase propagation of the pulses in the crystal. For the harmonic wave we find the following equation, the other two waves again having similar forms:

$$\frac{\partial E_{3}(\Delta\omega, z)}{\partial z} = ik_{3}(\omega_{3})E_{3}(\Delta\omega, z)
+ i\Delta\omega \left(\frac{\partial k_{3}(\omega)}{\partial\omega}\right)\Big|_{\omega=\omega_{3}} E_{3}(\Delta\omega, z)
+ i\frac{\Delta\omega^{2}}{2} \left(\frac{\partial^{2}k_{3}(\omega)}{\partial\omega^{2}}\right)\Big|_{\omega=\omega_{3}} E_{3}(\Delta\omega, z) + \dots
+ \frac{i\cdot(\omega_{3} + \Delta\omega)}{n_{3}(\omega_{3} + \Delta\omega)c} \int_{-\infty}^{\infty} d_{\text{eff}} E_{1}(\Delta\omega - \delta, z)E_{2}(\delta, z)d\delta,$$
(2.2.1)

where $E_j(\Delta\omega,z)$ is the electric field with the frequency difference $\Delta\omega$ from the central frequency of the respective wave. In contrast to the formulas in the book Crystal Nonlinear Optics [32], we choose $E_j(\Delta\omega,z)$ as the electric field and not as the complex electric field amplitude $\tilde{E}_j(\Delta\omega,z)=E_j(\Delta\omega,z)e^{ik_jcz}$ of the wave with the wave number of the carrier frequency $k_{jc}=k_j(\omega_j)$. This adds the first term in equation (2.2.1), representing the zeroth order phase propagation, and in turn removes the exponential function with the phase mismatch $e^{i\Delta k_cz}$ from the last term, the wave mixing term, as found in the book [32]. The leading terms in each of the three equations now incorporate the phase mismatch of the carrier waves into the simulation.

In my opinion, the form chosen in the book, obscures the fact, that the phase mismatch is not constant and can be different at any point in space and time during mixing. This is caused by the higher order dispersive effects, described by the first and higher order phase propagation terms. The physics is, of course, not changed by the different definition of the electric field symbol chosen in this thesis, but the mixing term does not suggest a wavelength independent phase mismatch.

We now want to make a few approximations in order to transform the mixing equations into the temporal domain. The effective nonlinearity is in general not constant over the entire bandwidth, but we will approximate it as constant for the bandwidths we use in this thesis. This simplifies the mixing equations as we can now write the effective nonlinearity outside the integral and the latter thus has the form of a convolution. We will additionally approximate

$$(\omega_j + \Delta\omega) \approx \omega_j \text{ and } n_j(\omega_j + \Delta\omega) \approx n_j(\omega_j) =: n_{jc}$$
 (2.2.2)

for j = 1, 2, 3. Fourier transforming equation (2.2.1) with the above approximations we can use the convolution theorem to rewrite the mixing equations in the time domain.

We thus have the electric field amplitudes $E_j(t,z)$ dependent on time t and the propagation distance in the nonlinear medium z. The mixing equations derived by Fourier transforming equation (2.2.1) using the given approximations have the form [32]

$$\frac{\partial E_{3}(t,z)}{\partial z} = ik_{3c}E_{3}(t,z) - \frac{1}{v_{g3}}\frac{\partial E_{3}(t,z)}{\partial t} - i\frac{D_{3}}{2}\frac{\partial^{2}E_{3}(t,z)}{\partial t^{2}} + \dots + i\frac{\omega_{3}d_{\text{eff}}}{n_{3c}c}E_{1}(t,z)E_{2}(t,z)
\frac{\partial E_{1}(t,z)}{\partial z} = ik_{1c}E_{1}(t,z) - \frac{1}{v_{g1}}\frac{\partial E_{1}(t,z)}{\partial t} - i\frac{D_{1}}{2}\frac{\partial^{2}E_{1}(t,z)}{\partial t^{2}} + \dots + i\frac{\omega_{1}d_{\text{eff}}}{n_{1c}c}E_{2}^{*}(t,z)E_{3}(t,z)
\frac{\partial E_{2}(t,z)}{\partial z} = ik_{2c}E_{2}(t,z) - \frac{1}{v_{g2}}\frac{\partial E_{2}(t,z)}{\partial t} - i\frac{D_{2}}{2}\frac{\partial^{2}E_{2}(t,z)}{\partial t^{2}} + \dots + i\frac{\omega_{2}d_{\text{eff}}}{n_{2c}c}E_{1}^{*}(t,z)E_{3}(t,z),
(2.2.3)$$

with the wave vectors k_{jc} and indices of refraction n_{jc} , the group velocities v_{gj} , the group

velocity dispersions D_j and the effective nonlinearity $d_{\rm eff}$, each on the respective central wavelengths.

The nonlinear mixing is again described by the rightmost term in each of the equations (2.2.3). In this form, in the time domain, they have the same form as the narrow band mixing equations (2.1.4) under the assumption of perfect phase matching, with the addition that the electric field is time dependent. Imperfect phase matching is incorporated more generally by the leading phase propagation terms instead of the complex phase from the phase mismatch in equation (2.1.4).

2.2.2 Dispersive Effects and Temporal Walkoff

The behavior of a laser pulse in a medium is governed by the dispersion relation $n(\omega)$ of the medium. In equation (2.2.1) the leading terms describe these dispersion effects on the pulses split into the different order effects such as the group velocity. They represent a Taylor series and can be rewritten to

$$\sum_{n=0}^{\infty} i \frac{\Delta \omega^n}{n!} \left(\frac{\partial^n k_3(\omega)}{\partial \omega^n} \right) \Big|_{\omega=\omega_3} E_3(\Delta \omega, z) = i k_3(\omega) E_3(\Delta \omega, z). \tag{2.2.4}$$

The book Crystal Nonlinear Optics [32] chooses the Taylor series in the equation in order to highlight the different dispersive effects taking place in broadband frequency conversion. In the form of equation (2.2.4) we can however more easily understand it as the phase propagation term of a wave. If we integrate the differential equation

$$\frac{\partial E_j(\omega, z)}{\partial z} = ik_j(\omega)E_j(\omega, z)$$
 (2.2.5)

with only the term from equation (2.2.4) we find the phase propagation of the wave over a propagation distance Δz as the exponential function

$$E_j(\omega, z + \Delta z) = E_j(\omega, z) \exp\left(i\frac{\omega n_j(\omega)}{c}\Delta z\right)$$
 (2.2.6)

with the index of refraction or dispersion relation $n_j(\omega)$ and j = 1, 2, 3.

For the understanding, however, of dispersive effects in broadband mixing, we will turn back to the form of equation (2.2.3) with the Taylor expansion terms of the phase propagation. These terms, of course, directly give us the different order dispersive effects occurring in broadband laser pulse propagation. We will quickly look at the three lowest

order effects, in order to better understand their impact on broadband frequency mixing later on.

The lowest or zeroth order phase propagation is simply the approximation that the index of refraction is constant for different laser frequencies. This implies that all frequency waves have the same phase velocity. It is a sufficient approximation if the bandwidth is sufficiently small as is the case in narrow band or monochromatic lasers. However, the different waves involved in frequency mixing can still have different phase velocities. In monochromatic SHG the phase velocity difference between the mixing waves is accounted for with the phase mismatch which we discussed in section 2.1.3.

For a laser pulse with a broad spectrum, we however need to take higher orders of the dispersion relation into account. Dispersion in the first order is called the group velocity [32]:

$$\frac{1}{v_a} = \frac{\partial k}{\partial \omega} \tag{2.2.7}$$

with the wave number k. As the name suggests, a wave packet will move with the group velocity v_g when propagating. If several wave packets are present, as is the case in broadband frequency doubling, unequal group velocities lead to a temporal walk-off of the pulses. Group velocities are typically different for pulses with different wavelength or polarization, but crystals with matching group velocities of the fundamental and harmonic pulses exist and are used to make efficient broadband SHG possible [55,56].

The second order dispersion is called the Group Velocity Dispersion [34]

$$GVD = \frac{\partial^2 k}{\partial \omega^2} \tag{2.2.8}$$

which generates a so-called chirp in the laser pulse. A chirp, in this case linear, causes the instantaneous frequencies at the start and end of a pulse to differ from the central frequency. This breaks the phase matching condition, as it is solely fulfilled for the central frequencies of the laser pulses. A reduction of conversion efficiency is thus expected if a significant chirp arises.

2.2.3 Incoherent Laser Pulses

Since the simulation of incoherent laser pulses is the topic of this thesis, I want to shortly define and outline the properties of incoherent laser pulses.

Coherence, as the opposite of incoherence is defined by the ability to generate interference. In order to do so, the phase difference of the wave at any two points in space must change

less than 2π for the duration of the observation [57]. We will call this a fixed phase relation. The important detail is, that we need a fixed phase relation for all combinations of two points in space. Coherence thus means, that, if we know the phase difference of the wave at two points in space at some time t, we know the phase difference of the wave at the same two points at the time $t \pm \Delta t_c$ has changed less than 2π . The time difference Δt_c , also called the coherence time, is defined as the maximum time for which the above property holds, that is, we find a fixed phase relation for all two-point combinations. The coherence time Δt_c is linked to the width of the frequency spectrum $\Delta \nu$ of the laser pulse by [58]

$$\Delta t_c \sim \frac{1}{\Delta \nu}.$$
 (2.2.9)

The fact that the phase difference may change for 2π might seem like a lot, but it is the value at which a maximum in the interference pattern decays to 1/e of its maximum amplitude [57].

With this, we can now define an incoherent pulse as a laser pulse which has a coherence time that is much smaller than the pulse length. Incoherence is thus not a binary property, as in, a pulse is either incoherent or not, but rather measured by the scale of the coherence time relative to the length of the pulse itself.

With the definition of coherence we can now take a look at the notions of spatial and temporal coherence. In both cases we take a look at the wave at two points restricted to an affine subspace in the mathematical sense. In spatial coherence this affine subspace is any plane perpendicular to the axis of propagation, meaning we choose two points that lie in the same plane. Temporal coherence is concerned with the affine subspaces parallel to the axis of propagation itself.

A spatially coherent laser pulse can for example be used to create interference patterns in a double slit experiment, where the two slits serve as the two spatial points chosen to observe the wave at. The measurement result is then seen on the screen as the interference pattern.

Temporal coherence on the other hand can for example be measured in a Michelson Interferometer. The spatial distance between two points along the axis of propagation is given by the path difference in the interferometer arms. As the wave propagates, any two points along the propagation axis with this distance will reach the screen to be measured.

In this thesis we will be concerned with pulses that are spatially coherent, that is, points in the planes perpendicular to the propagation axis have a phase relation that is fixed over the entire pulse length, but the pulses may be temporally incoherent, that is, their coherence time for points along the propagation axis is much shorter than the temporal length of the pulse. Such pulses are for example be generated by amplified spontaneous emission (ASE) in rare-earth doped fiber lasers [59] or by superluminescent LEDs [60]. These types of light sources are also used by other groups investigating incoherent broadband frequency conversion [25,61].

In order to produce incoherent laser pulses for the simulations we will numerically generate spectra with a random phase and amplitude for each frequency component [62]. The amplitude is bounded by an envelope and the phase is a random number between 0 and 2π . The resulting beam profile shows a temporal speckle with features around the size of the coherence time [57].

3 Laser Systems

In order to simulate SHG and verify the simulation and its results, we need physical measurements of SHG and more specific SHG with broadband laser pulses. The measurements used for this thesis have been conducted at the PHELIX facility. We will thus examine the details of the PHELIX laser relevant to the simulations. In order to get a broader view of the worldwide development of incoherent frequency mixing, we will however first look at other facilities conducting research in this field.

One of these facilities is the Laboratory for Laser Energetics (LLE) in Rochester. It is home to the OMEGA laser which is used for the study of laser plasma interaction and inertial confinement fusion. Current efforts in the field of incoherent frequency mixing include the development of the Fourth-generation Laser for Ultrabroadband eXperiments (FLUX) [63]. This laser is set to achieve a bandwidth greater than 10 THz and a pulse energy of around 100 J. The technology is based on the development of high-energy incoherent broadband optical parametric amplification [61] and the sum-frequency generation of spectrally incoherent pulses [28]. After completion, the FLUX beam will be transported to the target chamber of the OMEGA laser in order to conduct experiments concerning laser plasma instabilities [63].

The research setups, on which the FLUX is based, use ASE around a wavelength of $1053\,\mathrm{nm}$ from a doped fiber laser as an input. This is the seed pulse, which is then pumped in the OPA process by a monochromatic $1053\,\mathrm{nm}$ laser, frequency doubled to $526.5\,\mathrm{nm}$. The pumping is done using a non-collinear preamplifier OPA stage and a second, collinear OPA stage to achieve energies up to $400\,\mathrm{mJ}$ in pulses with a length of single nanoseconds and bandwidths up to around $16\,\mathrm{THz}$. The conversion efficiency from the pump to the signal pulse reaches up to 70% [61].

Near ultraviolet light is thereafter generated by mixing the incoherent broadband signal with another monochromatic frequency doubled laser at $526.5\,\mathrm{nm}$. Simulations yield an overall efficiency of this process up to 71% [28]. At this point only experiments with low intensities have been conducted, so high energy verification is still pending.

Another facility developing a low coherence laser with frequency conversion is the Kunwu facility in Shanghai [64]. The laser used here, the KUNWU laser, is an Nd:Glass laser operating at around 1053 nm. It is seeded by the ASE from a superluminescent diode which is preamplified in a fiber amplifier and subsequent Nd:glass rods. The main amplifier uses flash lamp pumped Nd:glass slabs, reaching energies up to the kilojoule regime with a bandwidth of 13 nm or 3.5 THz.

After that, the laser pulses are frequency doubled in a 15% deuterated DKDP crystal. The conversion efficiency is around 63% limiting the output energy to the upper $100\,\mathrm{J}$ to lower $1\,\mathrm{kJ}$ regime. The bandwidth after frequency conversion is nearly unchanged at $3.2\,\mathrm{nm}$ or $3.4\,\mathrm{THz}$ [64]. Measurements using a low aperture 15% DKDP crystal showed an efficiency up to 75% [55] implying potential improvements to the conversion efficiency at KUNWU and its output laser energy.

3.1 The PHELIX Laser

As stated in the introduction, this thesis is written in the context of the PHELIX laser. We will therefore use this chapter to also take a brief look at the parts important for the topic of this thesis in order to get a better understanding of the measurements and data presented here.

A schematic setup of the PHELIX laser is shown in figure 3.1.2. The laser pulses, which we will be concerned with, are nanosecond pulses which are generated in the nanosecond frontend. After pulse shaping and amplification in the pre- and main amplifier they are redirected to the designated beamlines and experimental areas. We will be concerned with the Z6 and HHT beamlines since both incorporate a nonlinear crystal for SHG. As diagnostic tools we will use the Main Amplifier Sensor (MAS) located after the main amplifier and the HHT Sensor located after the SHG crystal in the HHT beamline. Both these diagnostic systems make use of leaking light that passes a mirror in the main beamlines.

All measured data from PHELIX is subject to uncertainty. In order to retrieve reliable data from a simulation with this data as input we need to discuss these uncertainties.

The laser energy measurements at MAS and the HHT sensor have uncertainties of 3.2%. This is the combination of a 3% uncertainty of the detectors [65,66] and a 1% uncertainty of the measurement interfaces [67,68].

The camera at MAS measuring the near field of the laser pulse has a systematic error of 1.58% consisting of a nonlinearity of 0.5% and a photo response non uniformity of 1%.

These two errors affect the resulting spatial intensity profile of the pulse calculated from the near field image and the measured energy. Any pixel's intensity value can thus be over- or underestimated by this amount which results in an over- or underestimation of all other pixel values as well, since the pixel intensity values are normalized to the pixel sum.

3.1.1 Temporal and Spatial Parameters

The PHELIX laser has an Nd:glass main amplifier and thus operates at a wavelength of 1053 nm. With the nanosecond frontend, PHELIX can generate pulse lengths in the range of 0.7 to 20 ns with an energy up to 400 J [69]. We will mainly use pulse lengths around one nanosecond either assuming a flat top pulse profile or using the measured temporal profiles of the pulse. The MAS also provides measurements of the laser pulse intensity profiles (see figure 3.1.1 (a)) and their wavefront (see figure 3.1.1 (b)), which will be used for the simulations of harmonic conversion at the PHELIX facility.

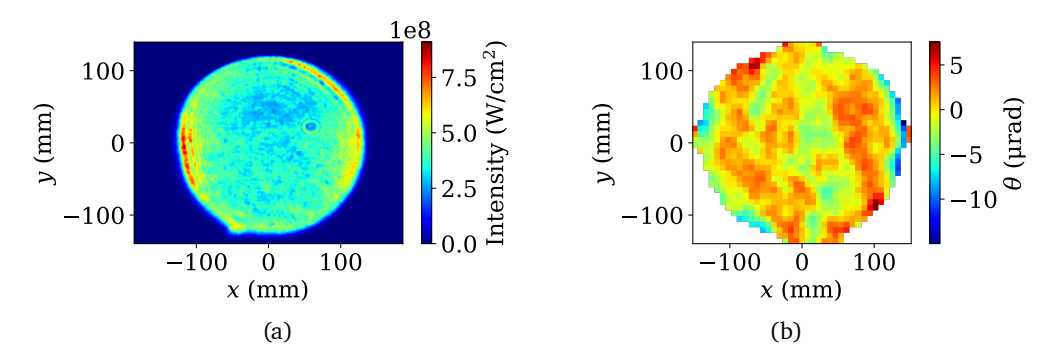


Figure 3.1.1: Intensity distribution (a) and angle deviation due to the wavefront imperfection (b) from shot number 18964.

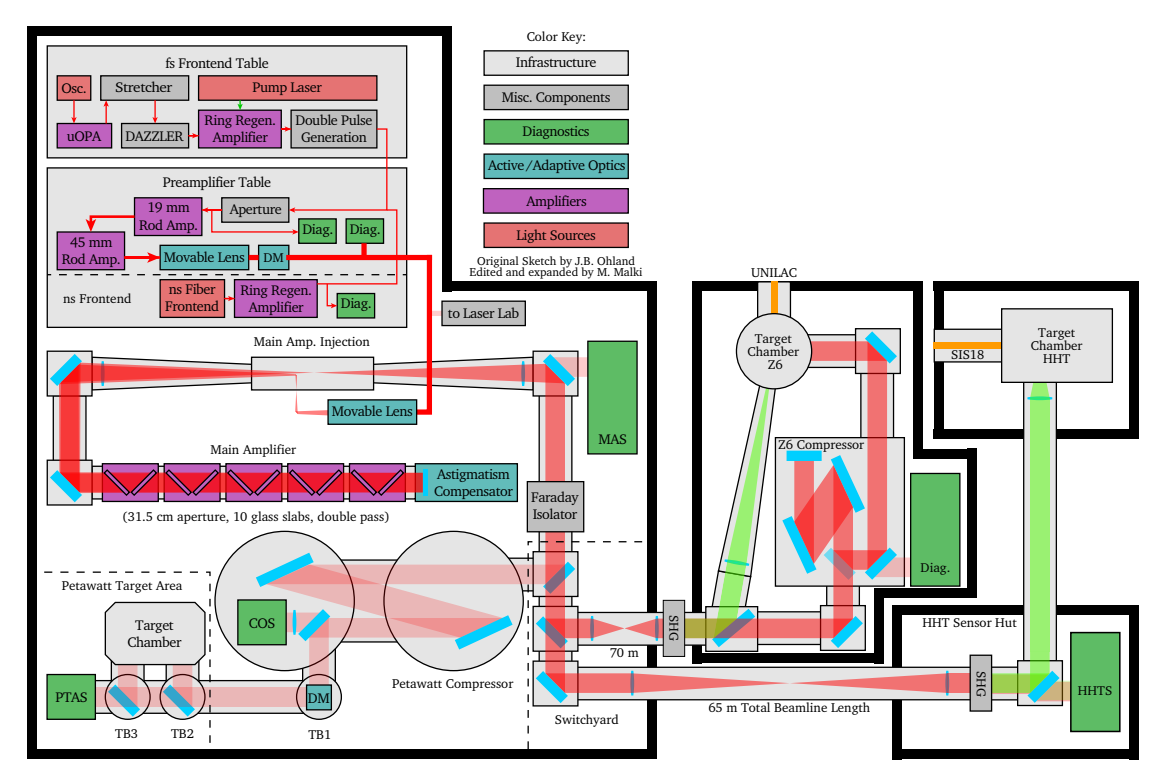


Figure 3.1.2: Schematic of the PHELIX laser system (extended, based on the sketch by J.B. Ohland [70]). The beam is created in the fs or ns frontend respectively, shaped by the pre-amplifier and then sent through the main amplifier. After traversing the main amplifier, the laser pulse is diagnosed at the Main Amplifier Sensor (MAS). An array of mirrors then redirects the laser pulse to its designated experimental area which is the Z6 or HHT area in our case since the beamlines to these areas incorporate a frequency doubling crystal each. The HHT beamline is equipped with another diagnostic setup, the HHT Sensor (HHTS), where for example the frequency converted energy is measured. Both the MAS and the HHT Sensor make use of leaking light from a mirror in the beamline.

3.1.2 Beamlines

The second-harmonic conversion of the laser pulses to 526.5 nm wavelength takes place in the beamlines to the experiment areas, namely the Z6 and HHT experiment areas.

The crystal in use at the Z6 beamline is a 70% deuterated DKDP crystal in type II phase matching configuration with a length of $25\,\mathrm{mm}$. The laser pulses have a diameter of around $25.8\,\mathrm{cm}$ at the crystal. Efficiency measurements of the frequency conversion have been conducted in the P203 experiment for several input energies, the results of which will be used in section 5.2 as a comparison to simulations.

The beamline to the HHT experiment area has been recently built and features a conversion crystal that is also a 70% deuterated type II DKDP crystal, but shorter at $17\,\mathrm{mm}$ length. The beam diameter lies around $15\,\mathrm{cm}$ at the crystal.

A part of the beamline commissioning was to measure the conversion efficiency of the implemented crystal, including measurements of beamline losses. The beamline allows for a placement of a power meter directly in front of the crystal, enabling the direct comparison between the energy measured at the MAS and the energy arriving at the crystal. This was used to measure beamline losses.

Final investigations and the data analysis concerning the topic of this work will constitute the next step after this thesis. Together with the measurement of the harmonic energy after the nonlinear crystal we can obtain a more detailed picture of the SHG that can then be reconstructed with the simulation code developed in this work.

4 SHG Simulation Tools

We will now discuss how to solve the mixing equations (2.1.4) for SHG in the case that all involved waves propagate collinearly. This can be done analytically [33,36] or by numerically solving the equations. The numerical solutions I present here are the simulation with the SNLO software [47] and the code written in the context of this thesis. The code developed in this thesis is capable of simulating SHG for monochromatic plane waves, monochromatic waves with arbitrary spatial intensity distributions and plane waves with an arbitrary spectrum.

4.1 Analytical Solutions

The monochromatic nonlinear mixing equations (2.1.4) can be solved analytically in the plane wave approximation [31]. Here we assume that the harmonic wave has zero energy before second-harmonic conversion, since that is the case in the setup at for example PHELIX and KUNWU. Additionally we want both fundamental waves to have the same input intensities. The intensities of the fundamental waves, as a side note, then stay equal throughout the entire mixing process, as photons of the fundamental waves are annihilated pairwise to create a photon in the harmonic wave (see Manley-Rowe relation in section 2.1.1). With these two assumptions the solution for the conversion efficiency takes the form [33]

$$\eta(L) = \left(\gamma^{(-)}\right)^2 \operatorname{sn}^2 \left[\gamma^{(+)} \frac{L}{L_{\text{NL}}}, \left(\gamma^{(-)}\right)^2\right] \tag{4.1.1}$$

where sn is the Jacobi elliptic function [71] and the following symbols are used:

$$\begin{split} \gamma^{(\pm)} &= \sqrt{1 + a^2} \pm a \text{ with } a = \frac{\Delta k L_{\rm NL}}{4}, \\ L_{\rm NL} &= \frac{1}{4\pi d_{\rm eff}} \sqrt{\frac{2\epsilon_0 n_{\omega,1} n_{\omega,2} n_{2\omega} c \lambda_{\omega}^2}{I_{\omega}(0)}}, \end{split} \tag{4.1.2}$$

with the effective nonlinearity $d_{\rm eff}$, the fundamental wavelength λ_{ω} , the input intensity at the fundamental wavelength $I_{\omega}(0)$ (both waves added) and the indices of refraction for the two fundamental waves $n_{\omega,j}$ and harmonic wave $n_{2\omega}$. The length $L_{\rm NL}$ is the scale length of the nonlinear interaction [33].

This general solution translates into the analytical solutions in the two limits commonly mentioned in literature [33, 36]. On the one hand this is the limit of perfect phase matching, that is $\Delta k=0$. With this we get a=0 and thus $\gamma^{(\pm)}=1$ in equation (4.1.2). When the second parameter of the Jacobi elliptic function is one, it equals the hyperbolic tangent [36] resulting in the form

$$\eta(L) = \tanh^2(L/L_{\rm NL}).$$
(4.1.3)

This function shows a saturation for large propagation distances and tends towards 1 for distances tending to infinity. In the lowest order, the efficiency is quadratically dependent on the propagation length L and linearly dependent on the input intensity.

The other limit is that of a large phase mismatch $\Delta k \gg 1/L_{\rm NL}$. This leads to $a \gg 1$ and therefore $\gamma^{(\pm)} \to a \pm a$. The second parameter in the Jacobi elliptic function is now zero, which brings it into the form of the sine function [36]. We use $\gamma^{(-)} = 1/\gamma^{(+)} \to 1/2a$ to find the conversion efficiency in the form [33]

$$\eta(L) = \left(\frac{L}{L_{\rm NL}}\right)^2 {\rm sinc}^2(\Delta k L/2). \tag{4.1.4}$$

In this case the frequency conversion does not saturate. We instead find an oscillation of energy between the fundamental and harmonic waves, its frequency depending on the phase mismatch and the amplitude depending on the input intensity.

We also want to take a quick look at the analytic solution if we assume one of the

fundamental waves to be stronger than the other, that is

$$\tilde{E}_1 \ll \tilde{E}_2. \tag{4.1.5}$$

We can herewith assume that the amplitude of wave \tilde{E}_2 does not change during mixing, that is $\frac{\partial \tilde{E}_2}{\partial z} = 0$. We will also call this the partial pump depletion scenario. This simplifies the mixing equations 2.1.4 to a simple set of two coupled differential equations

$$\frac{\partial}{\partial z}\tilde{E}_{1} = iK_{1}\tilde{E}_{3}e^{-i\Delta kz}$$

$$\frac{\partial}{\partial z}\tilde{E}_{3} = iK_{3}\tilde{E}_{1}e^{i\Delta kz}$$
(4.1.6)

with the real, positive constants K_1 and K_3 proportional to \tilde{E}_2 . Under the assumption that the fundamental wave is zero at input the equations 4.1.6 are solved by

$$\tilde{E}_3(z) = -\tilde{E}_1(0)\sqrt{\frac{K_3}{K_1}}\sin(\sqrt{K_1K_3}z).$$
 (4.1.7)

Especially we find an oscillation of energy between the weaker fundamental wave and the harmonic wave with the oscillation period proportional to the electric field amplitude of the stronger fundamental wave.

4.2 Numerical Tools

In this section we will take a look at some numerical tools for solving the mixing equations, namely the implementation in the SNLO software [47] and the tool developed in this thesis.

SNLO is a software, that offers numerical solutions to the nonlinear mixing equations (2.1.4) for several scenarios such as Gaussian or Super-Gaussian intensity profiles and pulse shapes. In section 5.1 we will use the solution offered by the SNLO software for the plane wave approximation to benchmark the code developed in this work.

The numerical code developed in this thesis works as follows. The mixing equations (2.1.4)

are ordinary differential equations as they can be written as

$$\frac{dy}{dz} = f(y, z). \tag{4.2.1}$$

An approach to solve such ordinary differential equations are the so-called finite difference methods, which is a general term for methods using a set of points $z_0, z_1, \ldots, z_m, \ldots$ and progressively calculating $y_m := y(z_m)$ from the values obtained at z_{m-1} [72].

We now use a fixed step size Δz to define this grid as $z_j = j\Delta z$. The simplest finite difference method is the Euler method defined by

$$y_{m+1} = y_m + \Delta z f(y_m, z_m). (4.2.2)$$

It uses the tangent $dy/dz|_{z=z_m}$ as an approximation of the function between z_m and z_{m+1} assuming a linear interpolation between these two points [72].

The Euler method is a first order method, which means, that the analytical error is of the order $\mathcal{O}(\Delta z^2)$. A higher order can be achieved by the classical Runge-Kutta method that is evaluated as

$$y_{m+1} = y_m + \frac{\Delta z}{6} \left(V_1 + V_2 + V_3 + V_4 \right) \tag{4.2.3}$$

with

$$V_{1} = f(y_{m}, z_{m}), V_{2} = f\left(y_{m} + V_{1}\frac{\Delta z}{2}, z_{m} + \frac{\Delta z}{2}\right),$$

$$V_{3} = f\left(y_{m} + V_{2}\frac{\Delta z}{2}, z_{m} + \frac{\Delta z}{2}\right), V_{4} = f(y_{m} + V_{3}\Delta z, z_{m} + \Delta z).$$
(4.2.4)

This method is of the order $\mathcal{O}(\Delta z^5)$ needing only linearly more evaluations of f than the simpler Euler method [72]. The code developed here thus uses the higher order Runge-Kutta method for solving the mixing equations (2.1.4).

The implementation is done with the so-called split-step method. In this method, the SHG is simulated by alternately calculating nonlinear wave mixing and linear wave propagation for each step of the computation. In the different simulations we consider different types of wave propagation. The narrow band simulation only considers spatial walk-off, which is only relevant in the two-dimensional case. The broadband simulation does not consider spatial propagation, but instead incorporates the phase propagation and its effects like for example group velocities.

The details will be further discussed in the sections concerning the respective simulations.

4.2.1 One-Dimensional Narrow Band Simulation - The Baseline

First, we want to look at SHG in the monochromatic plane wave approximation, the one-dimensional case. In this approximation we neglect all spatial properties of a laser beam that can have an influence on the SHG, like diffraction, walk-off or wavefront imperfections. We can therefore describe the entire laser pulse with a single intensity value at every point in the propagation direction.

We will consider absorption in the mixing process. The absorption is linear and is modeled with $I(z) = I(0)e^{-\alpha z}$ for some absorption coefficient α . In 70% deuterated DKDP crystals, which are used at PHELIX, the absorption coefficient is 0.4% cm⁻¹ for both ordinary and extraordinary waves at 1053 nm and 526.5 nm [73].

The implementation of the absorption is done as described in equation (2.1.8) as a linear term in the differential equation. A calculation via the split-step method is in this case thus not necessary and is done only with the Runge-Kutta method.

Two exemplary calculations using the parameters of the crystal at the HHT beamline at PHELIX (see section 3.1) are presented in figure 4.2.1. Figure 4.2.1 (a) assumes perfect phase matching and 4.2.1 (b) has a non-vanishing phase mismatch. The parameters used to calculate the intensity are a wavelength of $1053\,\mathrm{nm}$ in a pulse of $400\,\mathrm{J}$ energy, $15\,\mathrm{cm}$ beam diameter and 1 ns pulse length in a spatial and temporal flat top shape. Fringe effects are not considered. The crystal is a 70% deuterated DKDP crystal in type II configuration with a length of $17\,\mathrm{mm}$.

The simulation with perfect phase matching (see figure 4.2.1 (a)) shows a saturation of the harmonic wave energy while simultaneously depleting the fundamental wave energy. In the case of non-vanishing phase mismatch, the harmonic wave energy shows an oscillating behavior, the period of which is dependent on the magnitude of the phase mismatch. These examples reflect the expected behavior of the analytical solutions of the mixing equations, namely the saturation by the hyperbolic tangent for perfect phase matching and oscillation of the sine function in imperfect phase matching (see section 4.1).

In order to quantify the effect of imperfect phase matching on the conversion efficiency of a crystal, we simulate this exemplarily with the same parameters as before by varying the input angle and thereby also the phase mismatch. The results show a clear peak at the phase matching angle of $\theta=55.48^\circ$ which is set to zero in figure 4.2.1 (c).

The crystal at HHT has an acceptance angle FWHM of $737~\mu rad$ which is larger than the acceptance angle of the longer crystal at Z6 with $245~\mu rad$. This is because the longer crystal allows for back conversion of light from the harmonic to the fundamental wave for

smaller phase mismatch values as more total phase can be accumulated by the phasors over the length of the crystal.

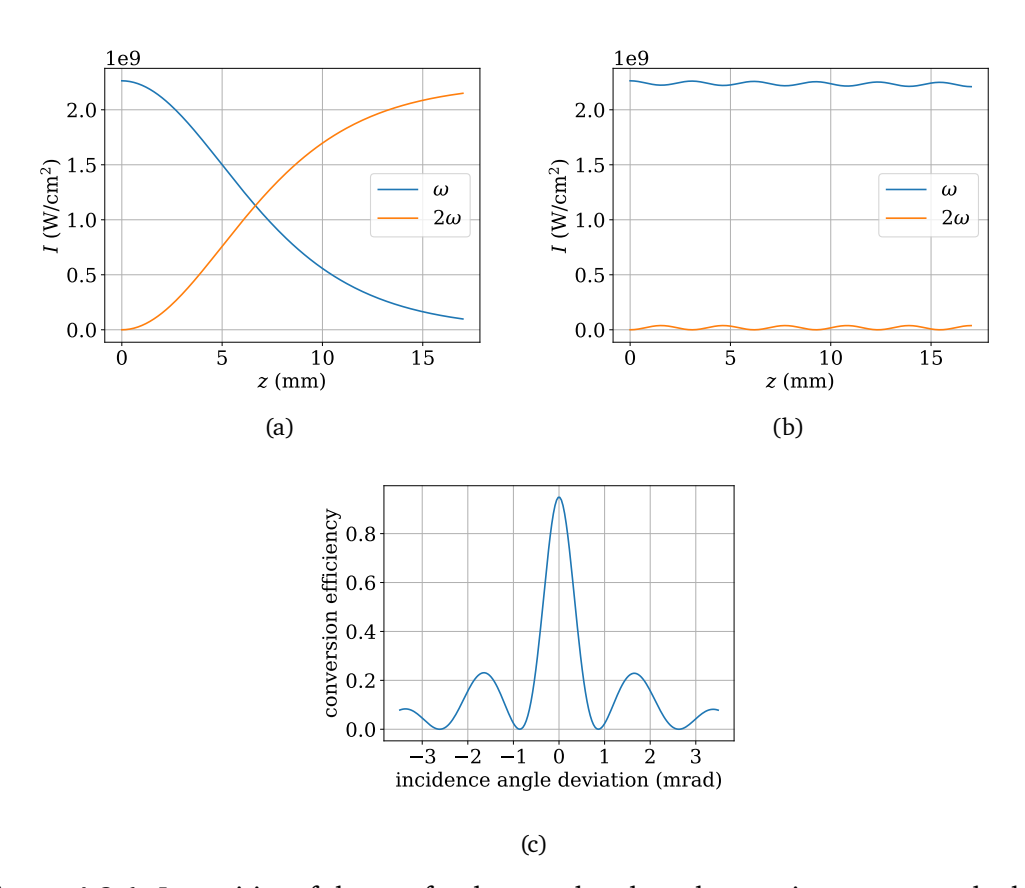


Figure 4.2.1: Intensities of the — fundamental and — harmonic waves over the length of the crystal with perfect phase matching in (a) and a mismatch of 2 mm⁻¹ (b). The crystal is a 70% deuterated DKDP crystal in type II configuration like the crystal used in the HHT beamline. In plot (c) the output conversion efficiency for varying angle of incidence and thus implicitly phase mismatch is shown.

4.2.2 Extension to Two-Dimensional Simulation

Now, we will expand our simulation from a plane wave to a beam with a two-dimensional intensity distribution perpendicular to the propagation direction of the beam. This is in particular interesting for simulating the second-harmonic output energy for PHELIX laser pulses. Besides the intensity distributions in the near field, PHELIX also provides other data on beam properties such as the wave front and the laser pulse energy, both of which we will use as input to the simulations of PHELIX laser pulses.

In this simulation we consider spatial walk-off, which will be calculated in the split-step method alternately with nonlinear mixing (see section 4.2). The nonlinear wave mixing is implemented in the same way as in the plane wave approximation, that is, the mixing equations (2.1.8) including linear absorption are solved, now however with electric wave amplitudes depending on the coordinates perpendicular to the propagation direction. This is equivalent to solving the mixing equations in the plane wave approximation for each point in the perpendicular plane.

In this simulation we will not take diffraction into account due to it significantly increasing computation times. As crystal lengths are in the order of centimeters or below, e.g. the crystal at Z6 is 25 mm long, and beam diameters can reach up to decimeters, e.g. the beam diameter at Z6 is around 26 cm, we cannot use the paraxial approximation to simplify the diffraction integral to the form of a convolution. Calculating the diffraction integral for high resolution electric field distributions is thus very time consuming in the order of minutes per step on a normal PC. In order to obtain short calculation times, we thus neglect diffraction entirely.

Spatial walk-off creates a shift of the intensity profile of the beam in the direction of the optical axis. The effect is implemented by shifting the image, that represents the intensity distribution of the beam, in the walk-off direction. Shifting in this case means moving the intensity distribution in the image relative to the image boundary. If the shift is not a whole number of pixels, the pixel data are interpolated with a third order spline.

In a 70% deuterated DKDP crystal the walk-off angles are between 1.25° and 1.5° for the fundamental and harmonic waves. This results in an overall walk-off of less than a millimeter for the crystals used at PHELIX.

A walk-off can in principle lead to a harmonic pulse with an intensity distribution, that is elongated in the walk-off direction compared to the fundamental wave [32]. Since the walk-off distance is much smaller than the diameter of the beam at PHELIX with around 15 cm, it has negligible effect on the geometry of the beam. It can however lead to reduced conversion efficiency if we take imperfect wavefronts into account.

The wavefronts incorporated into the simulations are wavefronts measured at PHELIX.

These are typically not perfectly flat wavefronts. This has two effects. Firstly, as by definition of a wavefront, the phase of the electric field in a plane perpendicular to the wave vector is not constant. Secondly, it leads to a slight distortion of the wave vector directions through the gradient of the wavefront.

The non constant phase is multiplied to the electric field amplitudes derived from the intensity distribution of the laser pulse's near field at the start of the simulation. This, in of itself, has no effect on the SHG except for creating a non flat wavefront in the harmonic output wave. If we combine this with spatial walk-off, we find areas of not matching phases drifting atop each other, effectively creating a phase mismatch.

An imperfect wavefront also results in wave vectors being slightly skewed in the direction of the gradient of the wavefront. Assuming that the incidence angle of the laser pulse is set such that the wave vector in a perfectly flat wavefront is perfectly phase matched, these skewed wave vectors evidently have a non-perfectly phase matched angle of incidence. As discussed in section 2, a deviation from the phase matching angle leads to a non-vanishing phase mismatch which, in turn, limits the maximum achievable conversion efficiency of the laser pulse.

In the simulation, we implement this by calculating the phase mismatch at every point of the intensity distribution depending on the gradient of the wavefront at the corresponding point. The code then uses this phase mismatch distribution with the intensity distribution for the simulation of second-harmonic wave mixing.

Wavefronts that are measured at PHELIX show an amplitude in the wavefront of at most several microns over the entire beam profile. The resulting deviations from the perfect phase matching angle have a standard deviation of less than $2.5\,\mu\text{rad}$ (see figure 4.2.2). Around 96% of wave vector angles are thus within $\pm 5\,\mu\text{rad}$ of the perfect phase matching angle. At $5\,\mu\text{rad}$ deviation from the phase matching angle the achievable conversion efficiency is around 0.2% below the maximum efficiency achieved at the phase matching angle.

We can also estimate the effect of the wavefront combined with walk-off. The gradient of the wavefront in the walk-off direction multiplied with the walk-off speed can be used to calculate a phase mismatch equivalent of the combined effect. For a typical PHELIX wavefront we find values for this quasi phase mismatch with a standard deviation of around $2\,\mathrm{m}^{-1}$ and thus around 96% of values within a spread of $4\,\mathrm{m}^{-1}$. A phase mismatch of $4\,\mathrm{m}^{-1}$ reduces the maximum achievable conversion efficiency by around 0.2%.

These estimates are consistent with simulation results. The difference in conversion efficiency between a simulation with and one without the two discussed effects lies below 0.1%.

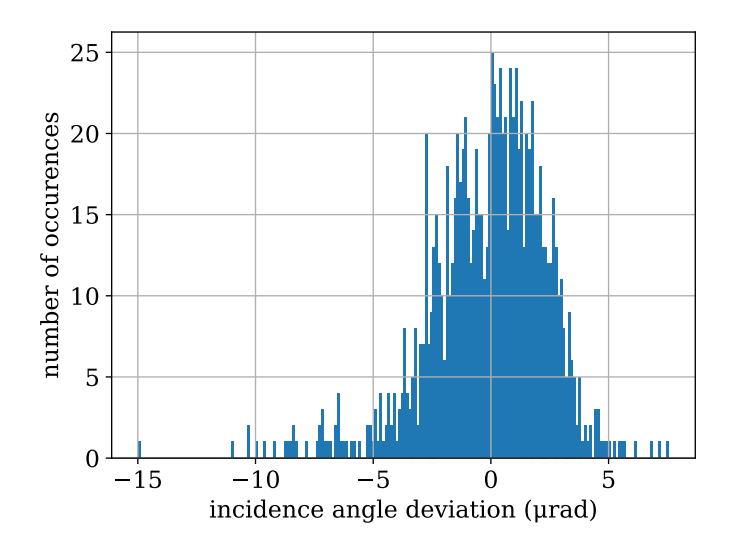


Figure 4.2.2: Histogram of the angle distribution of the wave vectors skewed by an imperfect wavefront in a typical wavefront at PHELIX. The gradient of the wavefront, and thereby the incidence angle, is calculated at each pixel in the image that represents the wavefront.

We will now take a look at an example of a two-dimensional simulation. The intensity distribution and wavefront used for this calculation were measured at the Main Amplifier Sensor (MAS) at PHELIX (see section 3.1).

As expected, the intensity distribution of the frequency doubled output (figure 4.2.3 (b)) shows similar features to the input distribution (figure 4.2.3 (a)). This is because the two-dimensional simulation can be viewed as quasi one-dimensional at every point in the intensity distribution. Walk-off in this case is significantly smaller than the beam diameter, thus not leading to a distortion of the harmonic intensity distribution. The output harmonic intensity is therefore correlated to the input fundamental intensity. In fact, features in the input intensity distribution, such as ripples, are expected to be more pronounced in the harmonic distribution. This is because points of lower input intensity achieve a lower conversion efficiency than the points of higher intensity and thus also have a relatively lower intensity in the output intensity profile.

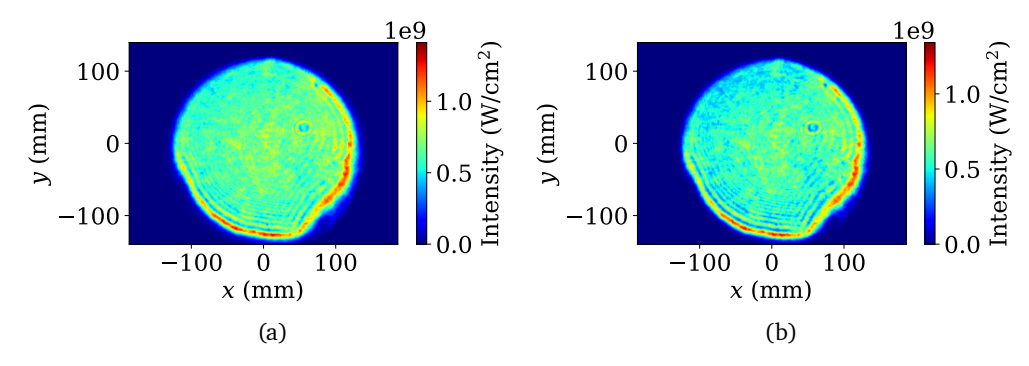


Figure 4.2.3: Intensity distributions for the input fundamental wave (a) and the second-harmonic wave after conversion (b). The simulation uses the intensity distribution from shot 19739 from the PHELIX database, assuming a 400 J and 1.2 ns long rectangle pulse converted with a 70% deuterated DKDP crystal of 25 mm length.

4.2.3 Extension of the Baseline to Broadband

With the toolset to simulate frequency doubling of narrow band laser pulses we will now turn toward simulations of pulses with non-zero bandwidth, which we will call broadband in this thesis. This extension of the one-dimensional simulation will enable us to investigate a large variety of laser pulses, as the initial spectral phase can be chosen deliberately to produce, for example, coherent pulses with a single temporal intensity peak or fully incoherent pulses with a randomly generated spectral phase.

The simulation is again using the plane wave approximation, enabling us to reduce the wave to a single value in space. However, broadband pulses are temporally structured, we thus need to consider a temporal window in which to simulate the laser pulses and their nonlinear interaction.

We will of course also be able to simulate narrow band laser pulses in this extension, as the initial spectrum can be chosen to be arbitrarily narrow. Combined with a short temporal window this generates an electric field that has constant amplitude to an arbitrary precision. This will serve as a way to verify the solutions we find for the differential equations 2.2.3 in this broadband case.

As described in section 2.2 we use the split step method for these simulations. The propagation part of the split step method will in contrast to the two-dimensional simulations not be the spatial walk-off but the phase evolution of the spectral components resulting

in dispersive effects including e.g. the temporal walk-off. The accuracy of this phase evolution solely relies on the accuracy of the Sellmeier equation used for the specific crystal. In our case for DKDP crystals we use an equation that is optimized for higher order terms [37]. The phase evolution is calculated using equation (2.2.6) in the frequency domain.

Nonlinear mixing is described in the time domain by equations (2.2.3) again with the terms for linear absorption added as in equations (2.1.8). The leading terms are ignored, as they are replaced with the phase propagation part of the split-step method.

Since the two parts are calculated in different domains, two Fourier transforms are necessary in every step of the simulation. This segues perfectly into a short description of the calculations done in each of the domains. Firstly, we find that the discrete Fourier transform directly links the frequency and time domains to each other. The number of data points in both domains is the same and they are linked by

$$T = \frac{1}{\Delta \nu} \text{ and } N = \frac{1}{\Delta t}$$
 (4.2.5)

with the total width of the temporal domain T and frequency domain N and the distance between two points in the temporal domain Δt and the frequency domain $\Delta \nu$. For clarification the total number of data points in each domain is $n = \frac{T}{\Delta t} = \frac{N}{\Delta \nu}$.

The waves are defined initially by their spectra. The code can in principal use any spectral shape, but we typically take either Gaussian curves or spectra from PHELIX shots as the initial spectra. If the coherence of the pulse needs to be lowered, a randomized phase can be applied to each of the spectral components in the frequency domain. In order to tune coherence continually, the random phase can be limited to have a phase difference below some maximum between neighboring spectral components.

The temporal profile, generated by Fourier transforming the spectrum, is then used to determine and rescale the pulse energy. Two possibilities for this are implemented in the code. The pulse can either be rescaled to have a certain peak intensity or a certain mean intensity. Peak intensity scaling is useful for comparing conversion properties of coherent pulses of different spectral widths. Mean intensity scaling on the other hand is more useful for comparing incoherent pulses, since the maximum intensity is subject to randomness.

In this section we will use the described simulation to survey different setups for broadband SHG using angular phase matching and determine the most promising one. For this we will first look at a number of different scenarios used in narrow band SHG and understand the effects that arise when applying them to broadband SHG. We will end on a type I scheme with matched group velocities of all involved waves, which is also the scheme

recommended by Gao et al. [25].

We start the investigation by examining the phase matching configurations type II and type I without and with group velocity matching. As a short reminder, type I uses an ordinarily polarized beam that is converted to an extraordinarily polarized harmonic beam. Type II has both an ordinary and an extraordinary fundamental beam, the harmonic beam again being extraordinary. The relevant aspect discerning the configurations in the context of broadband SHG is the mixture of group velocities of the involved waves.

4.2.3.1 SHG with Type II Phase Matching

In type II configurations all three waves, the ordinary and extraordinary fundamental waves as well as the harmonic wave, have different group velocities. This results in a temporal walkoff between each pair of waves. Due to this the conversion efficiency will be significantly reduced because the conversion strength is instantaneously proportional to the local field amplitudes of the fundamental waves (see Manley-Rowe Relation in section 2.1.1). Once the peak positions no longer coincide, the conversion strength decreases. In the case of coherent broadband laser pulses we have a single peak in each of the fundamental waves. After some propagation distance through the crystal, the fundamental waves will have drifted apart such that they do not overlap (see figure 4.2.4 (a)). Here frequency conversion to the second-harmonic ceases as can be seen in figure 4.2.4 (b).

Another effect that can be observed in the simulation of type II SHG is back conversion. In this case the back conversion does not however stem from a non zero phase mismatch but from unequal intensities of the fundamental laser pulses along the temporal axis of the pulses. When the fundamental pulses drift apart, there is always only exactly one point at which both waves have equal intensities. At every other point the intensities differ.

An analogous case with unequal intensities in the fundamental waves is described by the partial pump depletion scenario (see section 4.1). Here one fundamental wave is assumed to have a much weaker electric field than the other, leading to an oscillation of energy between the fundamental and harmonic waves with the period of the oscillation proportional to the amplitude of the stronger wave's electric field.

The same behavior can be observed in type II SHG where we can see both conversion from the harmonic to the fundamental waves with unequal intensities and depletion of the weaker fundamental wave leading to an amplification of the harmonic wave. An example of back conversion in the described scenario can be seen in figure 4.2.4 (b) as the decay of second-harmonic energy after conversion ceases. The smaller peak of the blue curve on the right is the product of this back conversion phenomenon.

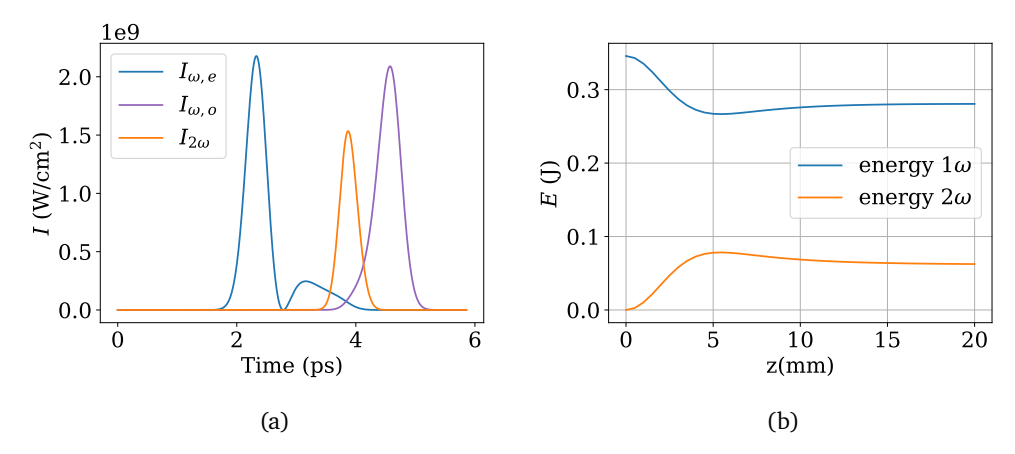


Figure 4.2.4: Simulation results for a broadband simulation in a type II phase matching setup with the temporal intensity profiles of the three involved pulses after propagation through a 20 mm crystal (a) and the energy balance of the pulses over the propagation distance (b). The input energy is 0.34 J at a bandwidth of 5 nm. The pulse is assumed to have a circular flattop as the spatial profile with a 15 cm diameter. The crystal used is a 70% DKDP.

4.2.3.2 Type I Phase Matching and Bandwidth Narrowing

In type I configurations, as compared to type II, the fundamental wave is solely ordinarily polarized in the crystal. We thus only have one fundamental wave and do not need to consider drifting of fundamental waves relative to each other. We can thus focus on the group velocity mismatch between the harmonic and fundamental wave.

We will first look at a crystal in which the group velocity mismatch is non-zero. This is for example the case for a 70% DKDP crystal at a central wavelength of $1053\,\mathrm{nm}$.

As stated in the Manley-Rowe relation (equation (2.1.7)), the change in the harmonic wave's electric field amplitude is proportional to the local amplitude of the fundamental wave. The maximum change in the harmonic field amplitude thus takes place at the position of the temporal intensity peak of the fundamental wave. However, while conversion takes place, the harmonic wave drifts away from the fundamental peaks position, producing a widened temporal pulse profile.

For low peak intensities the resulting harmonic wave has a relatively flat but slanted temporal profile (see figure 4.2.5 (a)). At higher intensities, once significant energy depletion

of the fundamental wave occurs, the slope of the harmonic wave becomes steeper with a trailing flank as can be seen in figure 4.2.5 (b). The lower ends of these flanks lie close to the remaining intensity peak of the fundamental wave.

The broadening of the harmonic pulse profile compared to the input fundamental wave's pulse profile has the effect that the output wave has a narrower spectrum than the input wave, since it has a lower Fourier limit. This effect of bandwidth narrowing is also described by A. V. Smith [32].

In the context of laser plasma interactions this is unfavorable. It has been shown, that spectrally broader laser pulses reduce or suppress the onset of laser plasma instabilities [27]. A reduction of bandwidth in turn increases the strength of laser plasma instabilities.

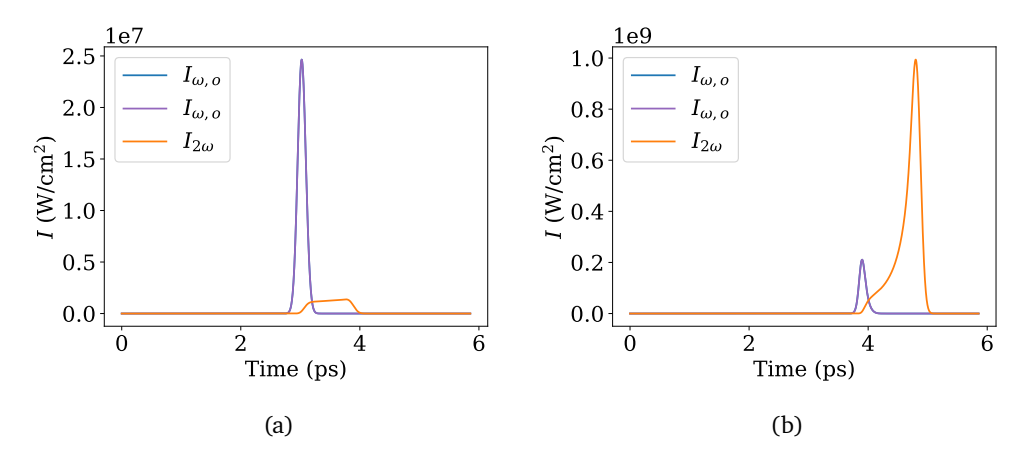


Figure 4.2.5: Simulation results for a type I phase matching configuration in a crystal with group velocity mismatch with pulse input energy of $0.4\,\mathrm{J}$ (a) and $16\,\mathrm{J}$ (b). The rest of the parameters are equal for both cases, namely a bandwidth of $10\,\mathrm{nm}$, a circular flattop profile with $15\,\mathrm{cm}$ diameter and a 70% DKDP crystal with a length of $50\,\mathrm{mm}$.

4.2.3.3 Group Velocity Matched and Phase Matched SHG

If we now assume, that the group velocities of fundamental and harmonic waves are equal, we can find SHG with high conversion efficiencies and stable bandwidths. Efficiencies of 55% [74], 56% [75] and 58% [56] have been reported experimentally in broadband SHG.

As stated in section 2.1.4, group velocity matching is achieved when a crystal has a vanishing first derivative of the phase mismatch

$$\left. \frac{\partial \Delta k(\omega, \theta(\omega_c))}{\partial \omega} \right|_{\omega = \omega_c} = 0 \tag{4.2.6}$$

at the phase matching angle of incidence θ for the central frequency ω_c . The wavelength at which the group velocity mismatch and the phase mismatch vanish is called the retracing point.

The above condition is met by different crystals for different wavelengths. For DKDP crystals with different levels of deuteration it is possible to reach wavelengths from $1034 \,\mathrm{nm}$ up to $1172 \,\mathrm{nm}$ [76] or $1034 \,\mathrm{nm}$ up to $1204 \,\mathrm{nm}$ [37] depending on the Sellmeier equations used. For the PHELIX laser operating at $1053 \,\mathrm{nm}$ the optimal crystal can be found to be a 15% deuterated DKDP crystal with type I phase matching [25].

We will again take a look at the relative positions of the intensity peaks of the laser pulses involved in the SHG mixing process. With matching group velocities these relative positions stay approximately constant over the propagation with only third or higher order dispersion terms having an influence. At each point along the temporal profile of the pulses the conversion thus approximately behaves like a one dimensional narrow band frequency conversion which we discussed and simulated before in section 4.2.1. If we assume phase matching and neglect higher order dispersion, the output wave can thus be calculated with the analytical solution to SHG (see section 4.1):

$$I_{2\omega}(t) = I_{\omega,0}(t) \tanh^2 \left(4\pi L d_{\text{eff}} \sqrt{\frac{I_{\omega,0}(t)}{2\epsilon_0 n_{\omega_0}^2 n_{2\omega_0} c \lambda_{\omega_0}^2}} \right), \tag{4.2.7}$$

with the input fundamental intensity profile $I_{\omega,0}(t)$, the length of the crystal L, the effective nonlinearity $d_{\rm eff}$ and the indices of refraction of the central wavelengths $n_{\omega_0,i}$. We especially find that depletion of the fundamental wave and thus efficient conversion can occur.

In regions with higher intensity the conversion strength is higher than at points of lower intensity. This leads to an earlier depletion of high intensity areas leaving a dip in the residual pulse at the position of the input peak. It also leads to a slight increase of bandwidth as the output harmonic pulse is temporally slightly shorter than the input fundamental pulse.

An example of the full simulation is shown in figure 4.2.6 (a). Here a pulse with a FWHM length of $161 \, \text{fs}$ and bandwidth of $3.8 \, \text{THz}$ is input into a $20 \, \text{mm}$ long, 15% deuterated

type I DKDP crystal. At a conversion efficiency of 81%, the output pulse has a length of $149\,\mathrm{fs}$ and a bandwidth of $4.4\,\mathrm{THz}$. The residual pulse is left with two peaks at either side of the initial Gaussian pulse and a dip in the middle.

A calculation with equation (4.2.7) of the same parameters yields results that deviate around 1% from the simulation results.

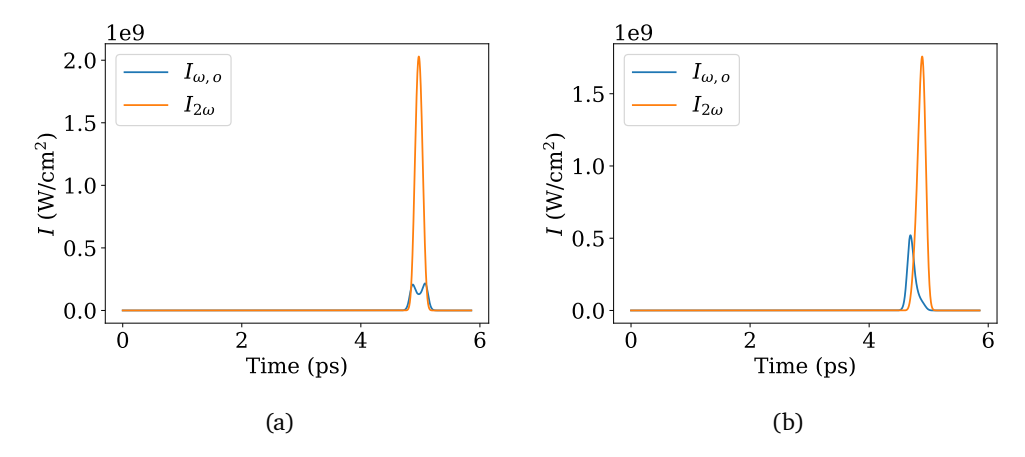


Figure 4.2.6: Simulation results for type I conversion with a 15% DKDP (a) and a 50% DKDP (b). The other parameters used are in both cases a pulse energy of 69 mJ, a bandwidth of 2.4 THz, a circular flattop profile with 15 cm diameter and a crystal length of 20 mm.

At this point, it can also be mentioned, that there is a tolerance to non-zero group velocity mismatch depending on the temporal width and intensity of the laser peaks. This is of course equivalent to the scenario discussed in section 4.2.3.2, but we find that under certain circumstances we can still achieve efficient conversion.

In order to achieve efficient conversion despite having group velocity mismatch, most energy needs to be converted before the packet of energy in the harmonic wave has drifted outside of the fundamental wave's peak. Otherwise conversion strength will be reduced, as it is also proportional to the harmonic wave amplitude (see Manley-Rowe Relation in section 2.1.1). A higher intensity pulse thus yields higher conversion efficiencies than a lower intensity pulse of the same bandwidth, since the higher intensity pulse undergoes conversion in shorter propagation distances.

As an example, a simulation with a 40% deuterated DKDP crystal is shown in figure 4.2.6 (b). This crystal has a group velocity mismatch of $8.29\,\mathrm{fs/mm}$ which results in an overall temporal delay of $166\,\mathrm{fs}$ after a $20\,\mathrm{mm}$ propagation. This is larger than the used FWHM

temporal width of $162\,\mathrm{fs}$ of the fundamental pulse. However, the conversion efficiency is still at 77% since the pulse intensity is high enough to quickly enough convert most of the energy.

4.2.4 Incoherent Broadband Pulses in Second-Harmonic Generation

After discussing broadband pulses in SHG in the case of coherent pulses we can now turn towards incoherent broadband laser pulses and the different behaviors they exhibit. We will again look at all three setups discussed in the previous section. This includes, of course, type I SHG with matched group velocities, as this is the most promising setup for efficient broadband SHG. The other two setups, type II and non group velocity matched type I SHG, show some differences in their behavior as compared to coherent pulses. These differences are due to the pulses being incoherent and can even lead to efficient frequency conversion in the latter two setups.

4.2.4.1 Incoherent Pulses in Non Group Velocity Matched SHG

Incoherent pulses in principle behave very similar to the coherent pulses discussed before. Their relative temporal positions are mainly dependent on the group velocities of the involved waves or rather the group velocity mismatch. The difference however is that incoherent pulses typically have multiple intensity peaks and troughs along the pulse length, the so-called temporal speckle (see figure 4.2.7 (a) for an example). Combined with the fact, that two points further apart than the coherence time have no fixed phase relation, we get two effects that cause the frequency conversion to have significantly different properties with incoherent pulses.

We will this time start with type I SHG, as only one of the effects we will discuss in this section is present in that case. Similar to coherent pulses, the peaks of the incoherent harmonic and fundamental pulses drift apart due to group velocity mismatch. Now however, after some more propagation through the crystal, a peak can start overlapping with an adjacent peak of the fundamental pulses again and increase the conversion strength. What we find, is that the conversion process can also transfer energy from the harmonic wave to the fundamental waves, if their phase relation changes. This can happen because of the temporal incoherence of the laser pulse.

As described in section 2.2.3, temporal incoherence means, that two points in time along the temporal axis of the laser pulse, which are further apart than the coherence time, have

no fixed phase relation. When drifting apart, the phase relation of the mixing waves at each point along the temporal profile thus changes. This is equivalent to areas of different phases overlapping due to spatial walk-off and hereby creating a phase mismatch (see two-dimensional simulation in section 4.2.2). This can lead to a transfer of energy back to the fundamental waves.

An example of this effect can be seen in figure 4.2.7 (b). The energy flow direction inverts after the temporal walkoff has surpassed the coherence time of 390 fs, which happens after a propagation distance of around 21 mm.

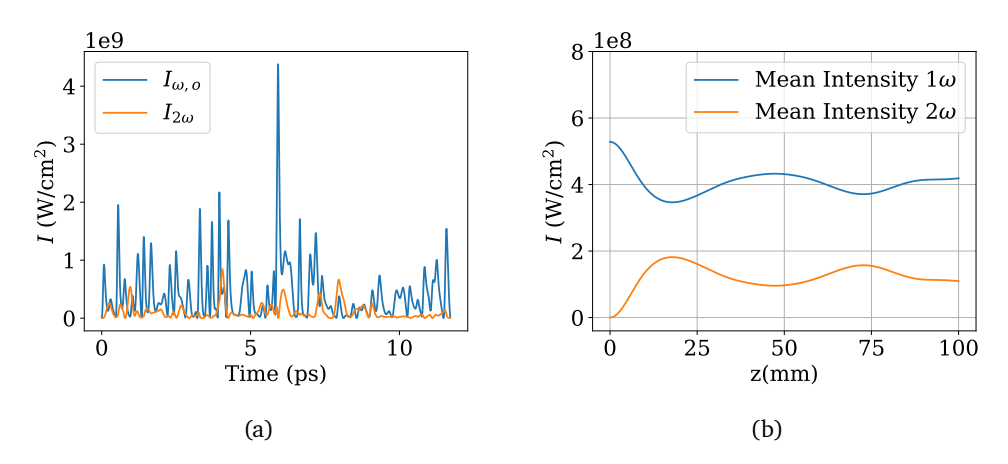


Figure 4.2.7: Intensities of fundamental and second-harmonic pulses over the temporal axis after conversion (a) and over the propagation distance (b) for a bandwidth of 10 nm. The crystal used in the simulation is a type I DKDP with a deuteration level of 70%.

We will continue by taking a look at SHG in a type II crystal. Here we have different group velocities for all three involved waves. Thus, the peaks of the fundamental waves as well as the emerging harmonic drift apart.

We find the same effects as in type I SHG, that is a decrease of conversion strength when peaks drift apart and an increase of it when peaks overlap with neighboring peaks of a different wave. This is also combined with the non fixed phase relation of peaks in the incoherent pulse, which can lead to a transfer of energy from the harmonic wave back to the fundamental waves.

We however find another effect that is due to the drift of the two fundamental waves against each other. Because of this we can encounter a situation where the harmonic peak overlaps with a peak of one of the fundamental pulses and a trough of the other one. This situation is equivalent to the back conversion effect described in section 4.2.3.1 for coherent broadband type II SHG. That means, depending on the phases of the three waves, we can observe a transfer of energy from the harmonic to the fundamental waves or the other way around.

Results of broadband type II simulations including all described effects can be seen in figure 4.2.8. The mean pulse intensity is herein subject to the effects happening at several peaks along the pulse simultaneously. As phases may vary along the temporal axis of the pulses, these effects can overlap constructively or destructively, arbitrarily leading to an increase, decrease or constancy of the mean pulse intensities. Depending on the exact pulse we can thus for example find stepwise increasing harmonic energy as in figure 4.2.8 (a) or decreases as in figure 4.2.8 (b). Overall these effects make for an unpredictable output of incoherent SHG in type II phase matching.

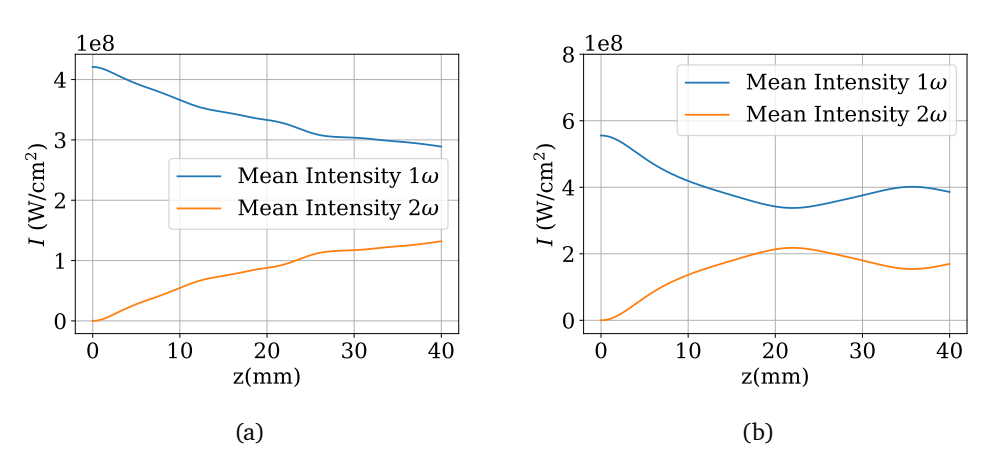


Figure 4.2.8: Pulse energies of fundamental and second-harmonic pulses over the propagation distance for bandwidths of 10 nm (a) and 5 nm (b). The crystal used in the simulation is a type II DKDP with a deuteration level of 70%.

4.2.4.2 Incoherent Pulses in Group Velocity Matched Type I SHG

As a finale we will look at a very promising setup for incoherent broadband SHG, as it eludes all of the efficiency limiting effects described before in this chapter: Group velocity matched type I SHG. Experiments with this type of SHG yielded up to 70% conversion efficiency for incoherent laser pulses [55].

The difference from this setup to before is, that the peaks do not drift apart. The conversion at each point along the temporal axis behaves approximately like in the one dimensional narrow band SHG. Up to the second order in the dispersion relation the conversion process can thus be described by equation 4.2.7. We find that this description can be useful at the start of the conversion process up to saturation. For example in a 15% deuterated DKDP crystal, SHG with pulses at a central fundamental wavelength of $1053\,\mathrm{nm}$ and a bandwidth up to around $10\,\mathrm{nm}$ fulfills the approximation quite well. The simulation yields a conversion efficiency up to 98% if the maximum intensity in the temporal speckle equals the damage threshold of the crystal of $18\,\mathrm{GW}/\mathrm{cm}^2$ at $1\,\mathrm{ns}$ pulse duration [77].

The approximation is no longer applicable after the conversion is fully saturated. At this point the instantaneous frequencies $\nu(t)$ of the laser pulse in the temporal axis have changed due to chirp induced by Group Velocity Dispersion (GVD), which is dispersion in the second order. This leads to a time dependent but in particular non zero phase mismatch $\Delta k(\nu(t))$.

We will again use narrow band SHG to explain the occurring effects. If we assume a marginally small but non-zero phase mismatch, SHG will exert a behavior where the conversion efficiency will almost reach one before inverting its behavior and transferring all the energy back to the fundamental waves. The propagation distance after which this inversion occurs depends on the magnitude of the phase mismatch. Since chirp generates different instantaneous frequencies along the temporal axis of the pulse, the phase mismatch is also different along this axis and thus back conversion will set in after different propagation distances for different points along the temporal axis. This way back conversion is averaged out and the harmonic pulse does not reach zero energy. If we use pulses that have a larger bandwidth, back conversion due to chirp will of course set in earlier, reducing the maximum efficiency reachable.

An example is given in figure 4.2.9 (a) where the mean intensity is around half the laser damage threshold of the crystal at 1 ns pulse duration. As can be seen, we have efficient frequency conversion in the first 9 mm of propagation after which back conversion sets in. The harmonic pulse does not however reach zero intensity due to the averaging effect described before. In fact, if linear absorption is neglected, the mean harmonic intensity in this example will settle to a fluctuation around a mean of $(4.6 \pm 0.1) \, \mathrm{GW}/\mathrm{cm}^2$ after around 50 mm propagation.

An interesting phenomenon appearing in the simulation alongside back conversion is bandwidth broadening. Back conversion will start in the regions where the instantaneous frequencies are furthest from the central frequency and thus where the phase mismatch is largest. These regions and the therefrom emerging peaks are shorter in time than the coherence time of the initial fundamental pulse. Because of the Fourier limit the resulting

harmonic peak thus needs to have a wider spectrum, which is exactly what the simulation results show.

The spectra for the above example of the output harmonic wave with a FWHM bandwidth of 7.6 THz as well as the input fundamental wave with a FWHM bandwidth of 2.2 THz are shown in figure 4.2.9 (b).

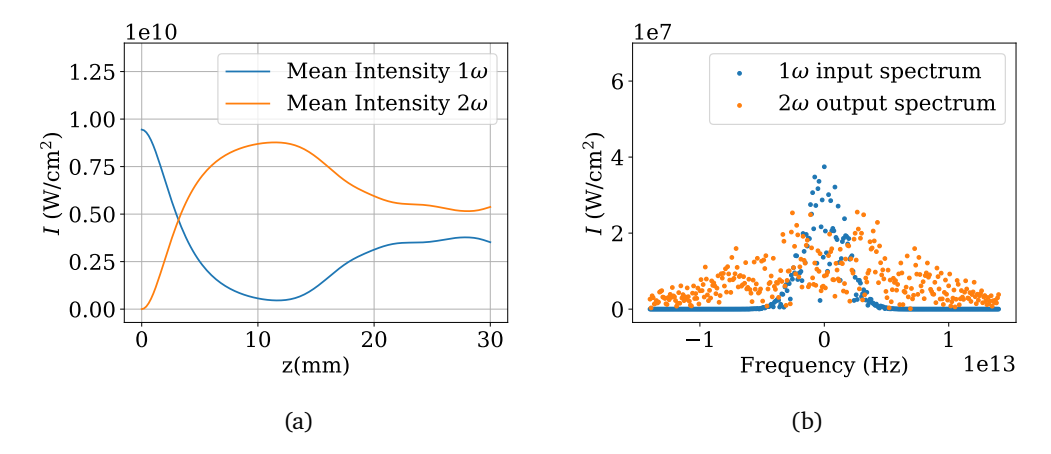


Figure 4.2.9: Mean pulse intensities of fundamental and second-harmonic pulses over the propagation distance (a) and the spectra of the fundamental input and harmonic output waves (b). The fundamental pulse has a central wavelength of $1053\,\mathrm{nm}$ and a bandwidth of $8.2\,\mathrm{nm}$ ($2.2\,\mathrm{THz}$) and is input into a 15% deuterated type I DKDP crystal. The harmonic output spectrum has a FWHM bandwidth of $7.6\,\mathrm{THz}$.

5 Simulation Verification

In this chapter we will take a look at the physical validity of the simulations done in this thesis. We will thus compare simulation results obtained in this thesis against results obtained by other means. For the one-dimensional narrow band simulation, these means are the SNLO software and the analytical solutions described in chapter 4.1. The two-dimensional simulation will be compared to actual measurements conducted at the PHELIX facility. Finally, the broadband simulations will be compared to the one-dimensional narrow band simulation of this thesis and also to the measurements carried out at the PHELIX facility.

5.1 Benchmarking of the One-Dimensional Narrow Band Simulations

We start by validating the one-dimensional narrow band simulations. For this we will utilize the results given by SNLO and the analytical solutions to the mixing equations 2.1.4. All three methods are input with the same parameters and the differences in the outputs will be investigated.

The simulation results from SNLO will likely have a comparably larger difference to this thesis' simulation results, as SNLO outputs its results only to an accuracy of around $1 \cdot 10^{-5}$. The analytical formulas (see equation 4.1.1) were fed with the exact same numerical values as the simulations from this thesis.

Simulation results of all three methods with exemplary physical parameters from PHELIX are shown in figure 5.1.1. The step size for the two numerical methods was chosen to be $5\,\mu m$ with phase mismatches of $\Delta k \in \{0\,mm^{-1},0.2\,mm^{-1},10\,mm^{-1}\}$. The difference between the three curves in figures 5.1.1 (a) and (b) is smaller than the width of the lines in the plot. In particular, the SNLO results differ less than 0.2% from the results of this thesis. The analytical solutions have a deviation of $1\cdot 10^{-14}$ for perfect phase matching

and around 1% for large phase mismatch.

We find a significantly larger deviation from our results in the case of a small non-vanishing phase mismatch. Here the error is visible in the plot. The reason for this deviation has not been determined yet, but it might stem from the analytical solution itself. A parameter fit of the analytical solution (equation 4.1.1) to the numerical curves has shown that the numerical results could be obtained analytically by taking the fourth power of the second parameter of the Jacobi elliptic function. This would then have the form

$$\eta(L) = \left(\gamma^{(-)}\right)^2 \operatorname{sn}^2\left[\gamma^{(+)} \frac{L}{L_{\text{NL}}}, \left(\gamma^{(-)}\right)^4\right]$$
 (5.1.1)

with the symbols defined in section 4.1. The deviation from the code developed in this work are reduced to below $1 \cdot 10^{-9}$ by this formulation for the phase mismatch cases. Why this different analytical formula appears and whether this could be the correct analytical solution has not been resolved yet. An analysis of the original paper by Armstrong et al. [31] and the book by R. L. Sutherland [33] could not uncover any mistakes or differing assumptions. For this thesis we will however neglect the analytical solution in this particular case since we find a good coincidence with the SNLO solutions. As, in the other two cases, the analytical solutions and the SNLO solutions coincide with the solutions given by the code from this work, we will assume the one-dimensional simulations from this work to be physically correct. This is not surprising as the limit cases are not affected by the exponent of the second term in the Jacobi elliptic function. In either case this factor tends to 1 for vanishing phase mismatch and to 0 for the limit of infinite phase mismatch leading to the same results.

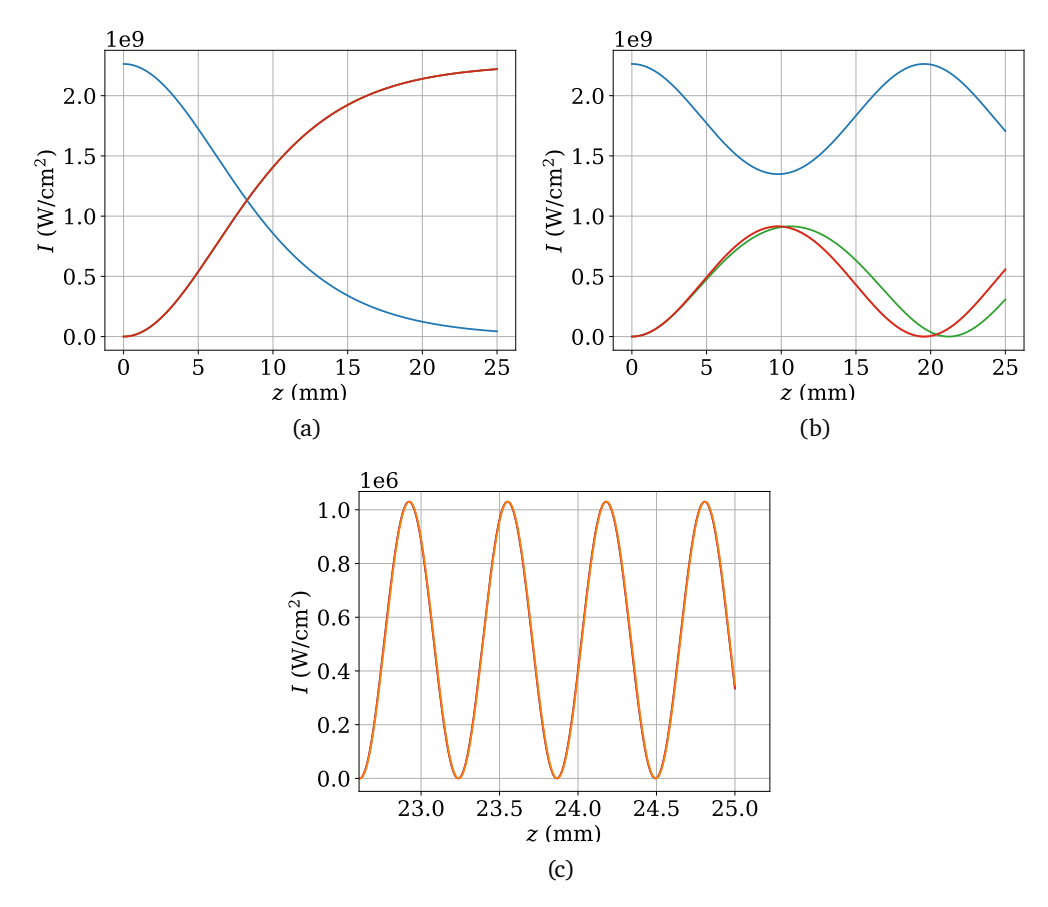


Figure 5.1.1: SHG calculations for perfect phase matching (a), phase mismatch of $0.2\,\mathrm{mm^{-1}}$ (b) and $10\,\mathrm{mm^{-1}}$ (c). The plotted curves are for — ω and — 2ω of the code from this work, — 2ω of the analytical solutions and — 2ω of the results given by the SNLO software. The pulse parameters are an input intensity of $2.3\,\mathrm{GW/cm^2}$ and a fundamental wavelength of $1053\,\mathrm{nm}$. The crystal used is a DKDP crystal with a deuteration of 70% and a length of $25\,\mathrm{mm}$ in a Type I configuration.

5.2 Two-Dimensional Simulations in Comparison to PHELIX Shots

The two-dimensional simulations allow for spatial intensity distributions in the plane perpendicular to the propagation direction of the laser beam. These can for example be the nearfield images measured at the PHELIX laser. With this simulation we can implement spatial effects like walk-off and imperfect wavefronts. Both the SNLO software and the analytical approach only provide solutions for simpler configurations. SNLO only solves the frequency doubling for certain spatial profiles such as a flat top or a perfect Gaussian. The analytical solution does not account for walk-off and imperfect wavefronts. They will thus inevitably return different solutions than the two-dimensional simulation done in this thesis.

For the comparison we will therefore use SHG efficiency measurements from the new HHT beamline instead. These measurements can be seen in figure 5.2.2 with the plain error bars.

The measurements are divided into the following three categories. The blue marks represent the first measurements as part of the beam time preparation. These include a pedestal in the temporal profile as well as an ASE background in the spectral profile. Both these features are shown in figure 5.2.1 (a) and (b) for clarification. The orange marks are a different set of measurements after the temporal pedestal was eliminated but the ASE background still present. Finally, the green marks were measured after both the pedestal and the ASE background were eliminated. For comparison, the temporal profile and spectrum of shots from these sets are also shown in figure 5.2.1.

The conversion efficiency values were calculated from the harmonic energy at the HHT sensor (HHTS), which is located after the crystal (see section 3.1.2), and the fundamental energy at the input face of the crystal. A prior measurement of the beamline transmission yielded a value of 0.9 that can be used to calculate the input energy from the fundamental energy value measured at the Main Amplifier Sensor (MAS).

The simulations use the calculated laser energy at the SHG crystal's input face as input. Additionally we need the temporal pulse profile, nearfield and wavefront of a laser pulse. These data are measured at the MAS but are used unchangedly as input data to the SHG simulation. Even though this does not take the propagation of the laser pulse through the beamline into account, the data from the MAS is the best available estimate for the actual

blue series: 21478 – 21484, 21487, 21489, 21490, 21508, 21509, 21513 – 21526, 21528, 21530 orange series: 21729 – 21731, 21733 – 21741

green series: 21747, 21748, 21751, 21754, 21758, 21763, 21767, 21769, 21772, 21773, 21777, 21780, 21782 – 21799, 21803, 21805, 21807, 21808, 21810, 21813

¹The PHELIX database shot numbers of the measurement series are as follows:

wavefront, nearfield and temporal profile of the pulses at the crystal's location.

The wavefront and nearfield are input into the simulation as described in section 4.2.2. The temporal pulse profile is not considered in the simulation itself but is used to define a set of input intensities. The calculation of the conversion efficiency for each PHELIX shot is thus comprised of multiple simulations for the different instantaneous intensities given by the temporal pulse profile. The overall efficiency is then calculated by adding the harmonic energy of all single simulations and comparing it to the total input energy. The underlying assumption is, that every point in the temporal profile can be represented by a temporally infinite pulse with constant intensity.

The simulation results are also included in figure 5.2.2 as the "corresponding simulations" to the measured sets of data. They are also plotted with the corresponding error bars. As can be seen, the results match the measured data points within the respective errors for the third (green) set without temporal pedestal and ASE background. The other two sets could not be entirely matched by the narrow band two dimensional simulation. The temporal pedestal was included in the calculations, the ASE background was not. For lower input energies, the simulation mostly aligns with the measurements within the respective error bars or lies within the fluctuation of the measurements among themselves. However above 53 J for the blue dots and above 63 J for the orange data, the simulation yields significantly higher conversion efficiency than measured. A possible reason for this behavior is the fact, that the ASE background, which is present for the blue and orange data points, was not included in this simulation. This might significantly influence the SHG conversion efficiency at higher energies.

The reason for the disparity in SHG efficiency appearing only at higher energy is that, at higher energies, the conversion strength is increased, which also leads to back conversion appearing after shorter propagation distances. For lower energies the back conversion also exists, but it would only set in at a propagation distance that is longer than the crystal itself.

The error bars of the measured data points consist of the errors of the measurement devices. As stated in section 3.1 these are 3.2% for a single energy measurement and thus 4.5% for the efficiency values. In the simulation we determine an uncertainty for the simulation results based on the same input energy error by simulating both the lower and upper end of the uncertainty of the input.

Also there is measured data that does not have a corresponding simulation result in the plot. In these cases the parameter set required to run a simulation was not complete or unusable for example due to noise in the temporal pulse profile.

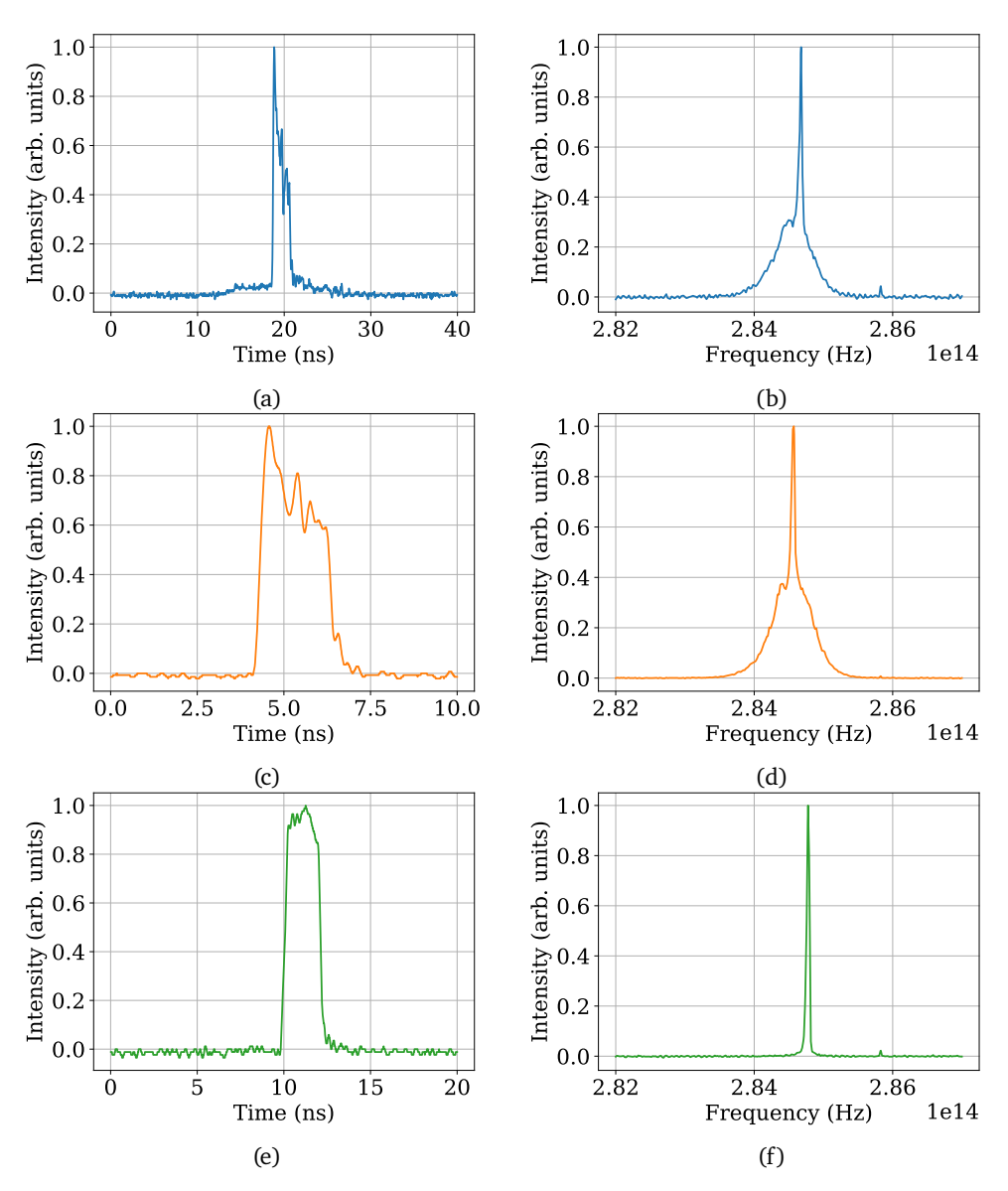


Figure 5.2.1: Examples of temporal beam profiles (a),(c),(e) and spectra (b),(d),(f) measured at PHELIX. These are exemplary for the three sets of measurements in the corresponding colors. Plots (a) shows the temporal pedestal and plot (b) the spectral ASE background from shot 21517 of the blue set. Plots (c) and (d) show the measurements for shot 21740 of the orange set, without temporal pedestal but with ASE. Plots (e) and (f) show the measurements without both temporal pedestal and ASE for shot 21813 of the green set.

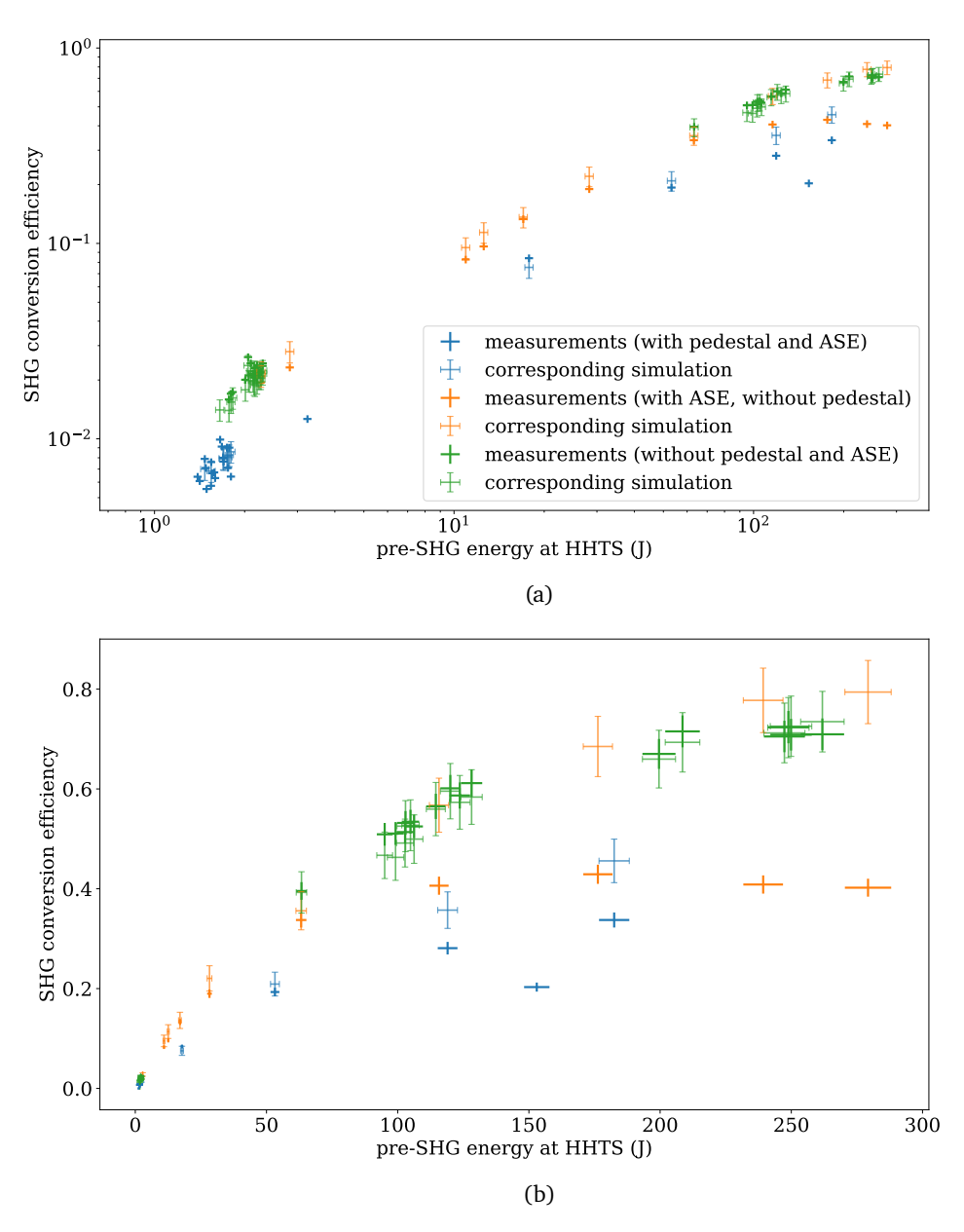


Figure 5.2.2: Measurements at HHT (plain, bold error bars) and corresponding two-dimensional narrow band simulations including temporal profile (error bars with serifs) where data is available. The plots display the same data in logarithmic (a) and linear scale (b).

5.3 Broadband Simulations in Comparison to PHELIX Shots

For the broadband case we will start by comparing the results of the simulation against the one dimensional narrow band simulation which we already verified. The spectrum in this case is chosen to be all zero except for one non zero point at a wavelength of 1053 nm. This produces a pulse with temporally constant intensity which matches the assumptions of the one dimensional case. We can thus compare these two cases and find that the intensities during conversion equal each other. Examples can be seen in figure 5.3.1 for an input intensity of $2.26\,\mathrm{GW/cm^2}$ and a 70% deuterated DKDP crystal in type I configuration. The curves differ from each other by less than $5\cdot10^{-6}\,\mathrm{W/cm^2}$ which is around 15 orders of magnitude smaller than the intensity of the input beam. We will thus assume the simulation to have a correct baseline.

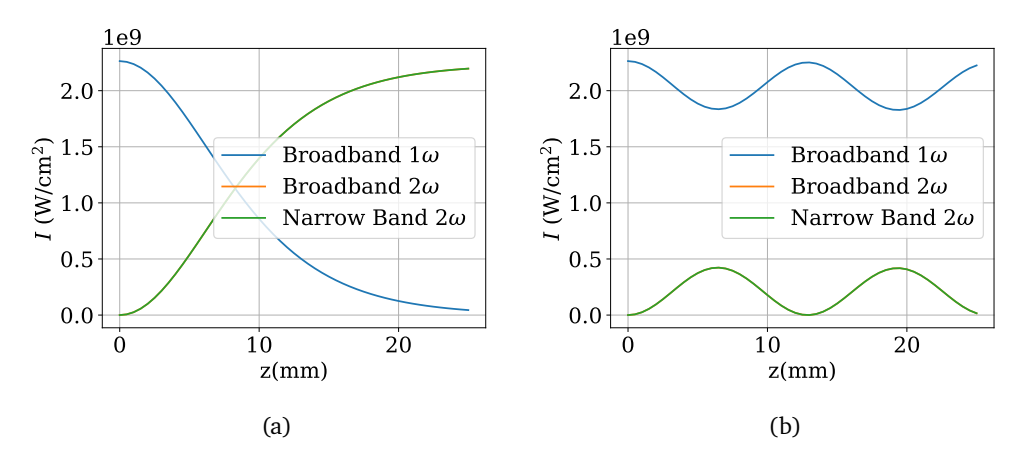


Figure 5.3.1: Wave intensities over propagation distance for perfect phase matching (a) and a phase mismatch of $0.4\,\mathrm{mm}^{-1}$ (b). The plotted curves are for — ω and — 2ω of the broadband simulation code and — 2ω of the narrow band simulation. The broadband simulation uses the single point spectrum described above and simulates in a temporal window $6\,\mathrm{ps}$ wide.

Further verification of the other scenarios covered by this simulation code is however necessary as the previous statement does not prove the broadband implementation correct. Currently no dedicated measurements have been conducted for broadband frequency conversion.

As stated in the above section 5.2 some measurements have however been done where an

ASE background was observed. Until further measurements will be conducted, these will be the measurements we will try to reproduce by simulation in this thesis.

The measured data is the same as in the comparison of two-dimensional narrow band in the section above (section 5.2). The corresponding simulations to the measurements are displayed in figure 5.3.2.

With the one-dimensional broadband simulation we take the pulse spectrum into account but neglect the nearfield and wavefront of the pulse. Since the measured spectrum does not contain phase information and is subject to measurement uncertainty, the temporal profile generated by Fourier transforming the spectrum does not resemble the measured temporal profile. We thus need to consider the measured temporal profile in the simulation, which we again do by simulating individually for every intensity point given by the temporal profile. Since the intensity along the temporal axis of each individual simulation is not constant, the given intensity is set to equal the mean intensity along the temporal axis. The resulting conversion efficiency has an uncertainty due to the randomness of the temporal speckle. For the simulations displayed in figure 5.3.2 we find an uncertainty of 2.6%.

As can be seen in figure 5.3.2 the broadband simulation was not able to reproduce most measurement data within the respective errors. The simulation results consistently underestimate the conversion efficiency. This is not expected as some aspects like the spatial pulse profile or imperfect wavefronts are not included in the simulation. Typically one would expect a higher conversion efficiency, if not all effects, that could lead to a reduced conversion efficiency, are included. This therefore suggests that some parameters are subject to systematic errors, which lead to a dramatic reduction of conversion efficiency.

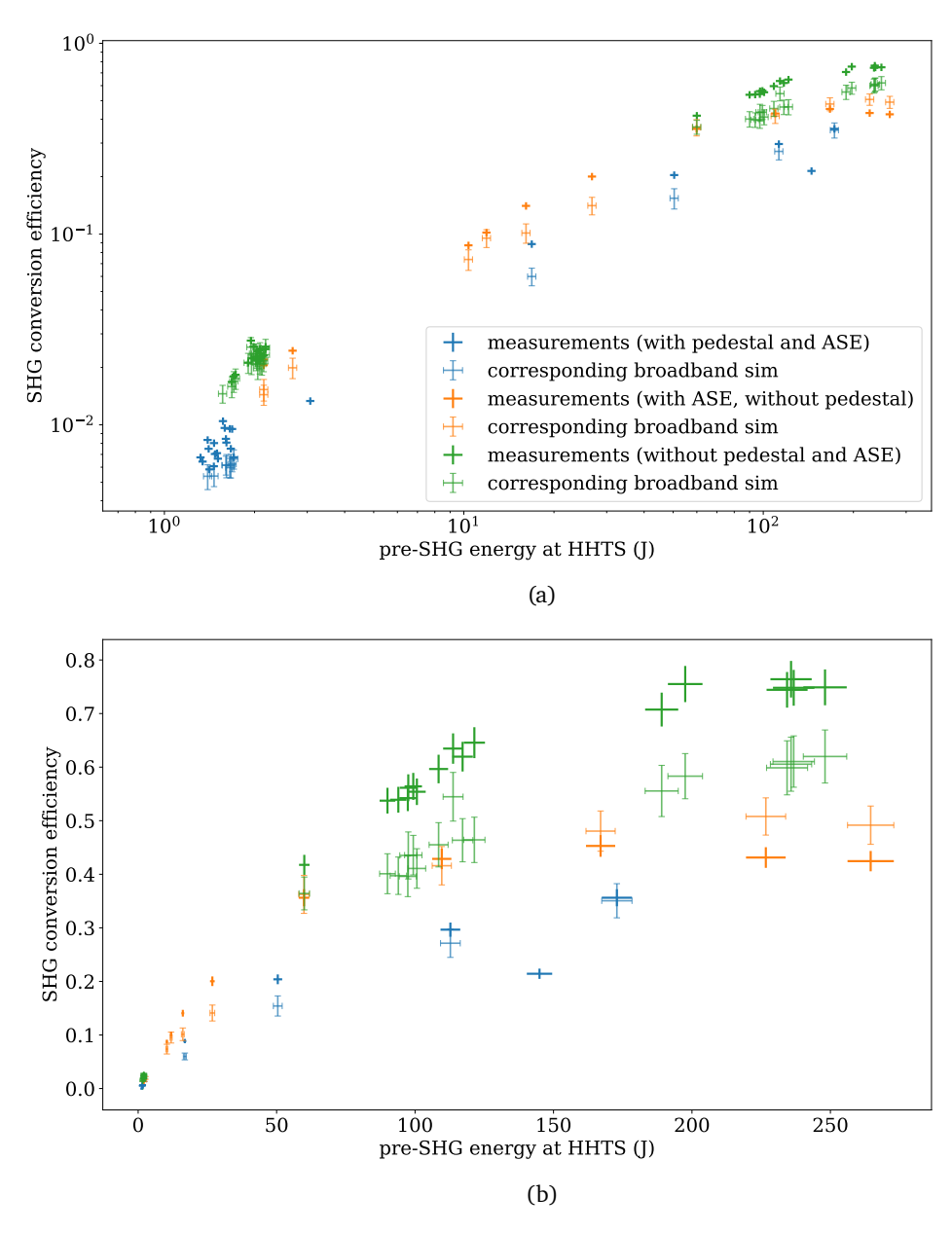


Figure 5.3.2: Measurements at HHT (plain, bold error bars) and corresponding one-dimensional broadband simulations including temporal pulse profile (error bars with serifs) where data is available. The plots display the same data in logarithmic (a) and linear scale (b).

A candidate for an improvable parameter is the input spectrum. The assumed coherent peak above the ASE background in the measured spectrum is expected to be far narrower than the measurement suggests. For a coherent pulse with a length in the order of single nanoseconds the spectral width calculates to an order of GHz. This is more than one order of magnitude below the minimal peak width measured at PHELIX of around 30 GHz. A possible explanation for this can be given by the fact that any measured spectrum is the convolution of the actual spectrum with the response function of the measurement device. If the response function is far broader than the spectral peak width, the measurement will also suggest a broader spectral width.

A correction of this fact was implemented into the simulation. The measured spectrum is fitted to a function that is the sum of two Gaussian curves. The broader Gaussian curve in this fit is herein assumed to represent the ASE background, that is present in some of the PHELIX shots, as described before. The narrower Gaussian curve on the other hand is assumed to represent the coherent part of the spectrum. This coherent part is then transformed to a peak with a narrower width but the same total energy. This changes the ratio between the field amplitudes in the coherent part of the spectrum and the incoherent ASE as the electric field amplitude, being the relevant factor in the simulation, is proportional to the square root of the intensity.

The simulation results with this correction implemented can be seen in figure 5.3.3. The width chosen for the narrowed peak is 6 GHz. The blue series is entirely matched by the simulation within the respective uncertainties. In the orange we find a coincidence for all but the two highest energy shots, which are slightly overestimated by the simulation. The discrepancy is however much smaller than without the spectral correction (see figure 5.3.2) or in the two-dimensional simulation results (see figure 5.2.2). Lastly the green series is overestimated in all shots up to an input energy of 60 J. Above this input energy the error bars of the measurements and simulations overlap. With most measured data points matched by the simulation results, we will conclude that the simulation with the correction of the spectral width yields physically correct results. Moreover we can conclude that the shots with ASE are more accurately replicated by the broadband than the two-dimensional simulation.

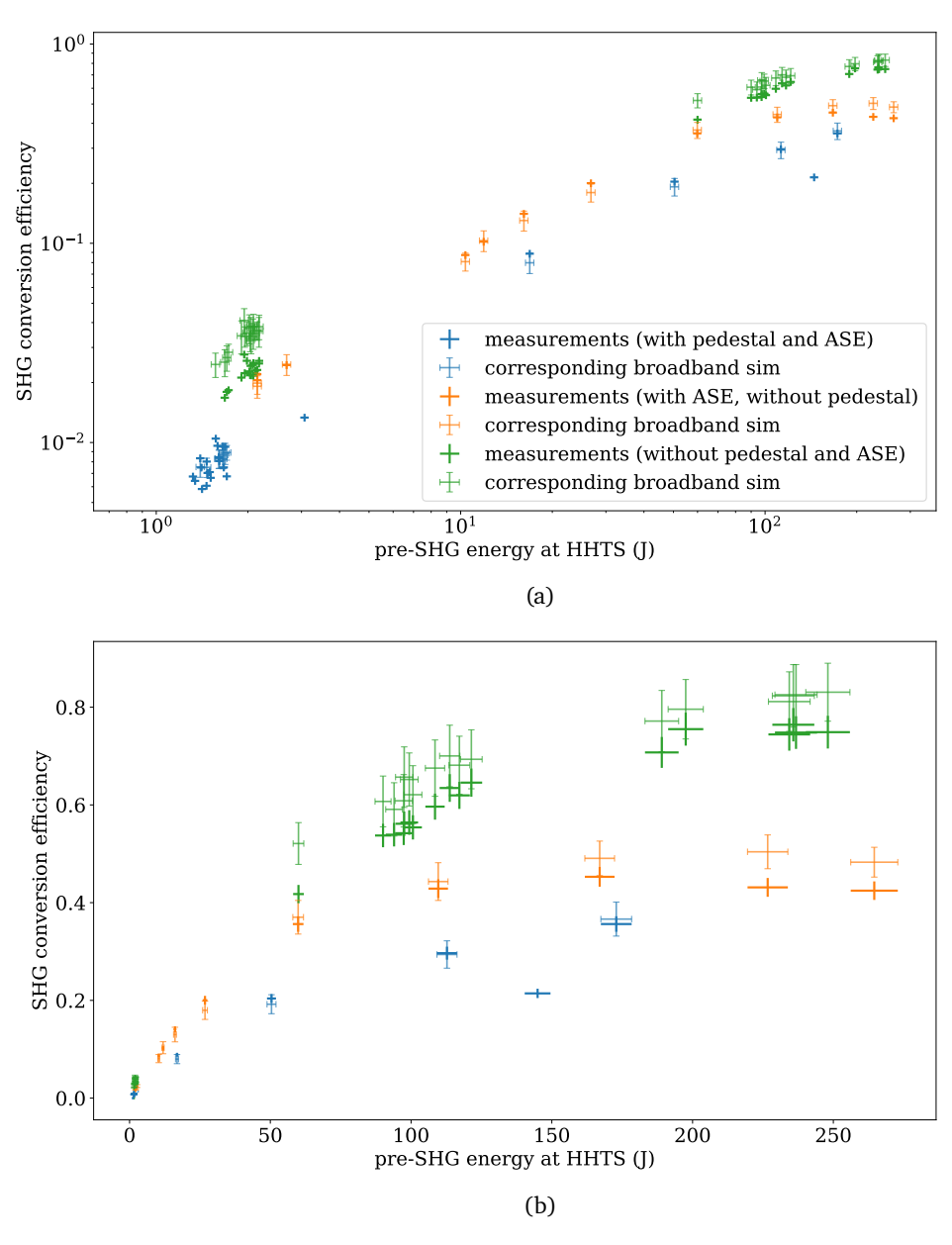


Figure 5.3.3: Measurements at HHT (plain, bold error bars) and corresponding one-dimensional broadband simulations, where data is available, including temporal pulse profile and a correction of the coherent part of the spectrum (error bars with serifs). The plots display the same data in logarithmic (a) and linear scale (b).

6 Summary & Outlook

In this thesis a tool for simulating Second-Harmonic Generation (SHG) with narrow band and broadband, especially incoherent broadband, laser pulses was successfully developed. The narrow band code is able to incorporate pulse properties such as the the spatial shape and the wavefront together with effects such as spatial walkoff in birefringent crystals. In the broadband case the spectrum of the pulse is included and simulated with the occurring dispersive effects. Both codes can be used to simulate the temporal profile of a pulse.

The code developed in this thesis was verified to yield physically correct results. Firstly the narrow band simulations were compared to established solutions to the SHG mixing equations (2.1.4), namely the analytical solutions and the SNLO software. Both were found to have a deviation of less than 1% to the results of this thesis' simulation.

The two-dimensional narrow band as well as the broadband simulation were compared to a set of measurements that were conducted at the HHT beamline at the PHELIX laser facility. These measurements included laser shots, that incorporated an ASE background, and shots without ASE. The two-dimensional narrow band simulation was able to match the measurement data of the shots without ASE within the respective uncertainties. The shots with ASE could be reproduced with the broadband simulation within the respective uncertainties. The broadband simulation was moreover capable of matching the measurement data of the narrow band PHELIX shots with energies above $60\,\mathrm{J}$.

We can thus conclude that both the narrow band and broadband simulations yield physically valid results and that the broadband simulation can also be useful in narrow band cases.

The thesis discussed different effects occurring in the SHG with broadband lasers in type I and II phase matching setups in more detail. Various effects leading to conversion of energy from the harmonic wave back to the fundamental waves were discussed. These effects stem from group velocity mismatch with and without incoherence as well as frequency chirp and limit the overall conversion efficiency of broadband SHG. This discussion is

concluded by investigating the properties of the type I phase matching setup with matching group velocities, which is a very promising setup for incoherent broadband SHG [25].

There is a need to conduct further experiments with broadband and incoherent broadband laser pulses in order to better understand and verify the existence of the various occurring effects described in this thesis. For this another SHG crystal will be ordered, specifically a type I phase matched 17% deuterated DKDP crystal. This crystal sufficiently fulfills the criterion of matched group velocities for a central wavelength of 1053 nm which, supported by the simulation, enables high efficiency broadband SHG.

Additionally the capability to generate high energy incoherent broadband laser pulses needs to be implemented into the PHELIX laser system. A possibility for this is a free running, or not seeded, regenerative amplifier, that outputs high intensity ASE. Other possibilities discussed in the literature are superluminescent LEDs [64] rare-earth doped fiber amplifiers [59].

A dedicated ASE generating capability and the described crystal will enable the PHELIX laser to generate incoherent broadband second-harmonic laser pulses, that can then be used to further investigate laser plasma instabilities and their suppression with broadband lasers. This is an important step towards enabling stable and efficient laser-plasma coupling which can for example smooth the path toward ICF.

Bibliography

- [1] C. Labaune, Incoherent light on the road to ignition, Nat. Phys., **3**:680–682, 2007, doi:10.1038/nphys742.
- [2] G. Zimmerman, A. Thiessen, L. Wood *et al.*, Laser Compression of Matter to Super-High Densities: Thermonuclear (CTR) Applications, Nature, **239**:139–142, 1972, doi:10.1038/239139a0.
- [3] J. Ongena, R. Koch, R. Wolf *et al.*, Magnetic-confinement fusion, Nat. Phys., **12**:398–410, 2016, doi:10.1038/nphys3745.
- [4] R. S. Craxton, K. S. Anderson, T. R. Boehly *et al.*, Direct-drive inertial confinement fusion: A review, Phys. Plasma, **22**(11):110501, 2015, doi:10.1063/1.4934714.
- [5] E. I. Moses, R. N. Boyd, B. A. Remington *et al.*, The National Ignition Facility: Ushering in a new age for high energy density science, Phys. Plasma, **16**(4):041006, 2009, doi:10.1063/1.3116505.
- [6] J. Lindl, Development of the indirect-drive approach to inertial confinement fusion and the target physics basis for ignition and gain, Phys. Plasma, **2**(11):3933–4024, 1995, doi:10.1063/1.871025.
- [7] S. Atzeni and J. Meyer-ter Vehn, The Physics of Inertial Fusion, Oxford University Press, 2009, doi:10.1093/acprof:oso/9780198562641.001.0001.
- [8] J.-L. Miquel, C. Lion and P. Vivini, The Laser Mega-Joule: LMJ & PETAL status and Program Overview, J. Phys. Conf. Ser., 688:012067, 2016, doi:10.1088/1742-6596/688/1/012067.
- [9] J. D. Lindl, R. L. McCrory and E. M. Campbell, Progress toward Ignition and Burn Propagation in Inertial Confinement Fusion, Physics Today, **45**(9):32–40, 1992, doi:10.1063/1.881318.

- [10] S. Le Pape, L. F. Berzak Hopkins, L. Divol *et al.*, Fusion Energy Output Greater than the Kinetic Energy of an Imploding Shell at the National Ignition Facility, Phys. Rev. Lett., **120**(24):245003, 2018, doi:10.1103/PhysRevLett.120.245003.
- [11] C. Labaune, E. Fabre, C. Max *et al.*, Effect of Laser Wavelength and Pulse Duration on Laser-Light Absorption and Back Reflection, Phys. Rev. Lett., **48**(15):1018–1021, 1982, doi:10.1103/PhysRevLett.48.1018.
- [12] F. Dahmani and T. Kerdja, Laser-intensity and wavelength dependence of mass-ablation rate, ablation pressure, and heat-flux inhibition in laser-produced plasmas, Phys. Rev. A, **44**(4):2649–2655, 1991, doi:10.1103/PhysRevA.44.2649.
- [13] P. A. Franken, A. E. Hill, C. W. Peters *et al.*, Generation of Optical Harmonics, Phys. Rev. Lett., **7**(4):118–119, 1961, doi:10.1103/PhysRevLett.7.118.
- [14] R. S. Craxton, High Efficiency Frequency Tripling Schemes for High-Power Nd:Glass Lasers, IEEE J. Quantum Electron., 17(9):1771–1782, 1981, doi: 10.1109/JQE.1981.1071318.
- [15] E. Fabre, A. M. Tournade and D. Bruneau, Fourth harmonic generation of a large-aperture Nd:glass laser, Applied Optics, **24**(22):3740–3745, 1985, doi: 10.1364/AO.24.003740.
- [16] I. A. Begishev, R. A. Ganeev, A. A. Gulamov *et al.*, Generation of the fifth harmonic of a neodymium laser and two-photon absorption in KDP and ADP crystals, Sov. J. Quantum Electron., **18**(2):224–228, 1988, doi:10.1070/qe1988v018n02abeh011480.
- [17] D. S. Montgomery, Two decades of progress in understanding and control of laser plasma instabilities in indirect drive inertial fusion, Physics of Plasmas, **23**(5):055601, 2016, doi:10.1063/1.4946016.
- [18] G. I. Taylor, The instability of liquid surfaces when accelerated in a direction perpendicular to their planes. I, Proc. R. Soc. London, Ser. A, **201**(1065):192–196, 1950, doi:10.1098/rspa.1950.0052.
- [19] K. A. Brueckner and S. Jorna, Laser-driven fusion, Rev. Mod. Phys., **46**(2):325–367, 1974, doi:10.1103/RevModPhys.46.325.
- [20] S. Skupsky, R. W. Short, T. Kessler *et al.*, Improved laser-beam uniformity using the angular dispersion of frequency-modulated light, J. Appl. Phys., **66**(8):3456–3462, 1989, doi:10.1063/1.344101.

- [21] Y. Kato, K. Mima, N. Miyanaga *et al.*, Random Phasing of High-Power Lasers for Uniform Target Acceleration and Plasma-Instability Suppression, Phys. Rev. Lett., 53(11):1057–1060, 1984, doi:10.1103/PhysRevLett.53.1057.
- [22] J. H. Gardner and S. E. Bodner, Wavelength Scaling for Reactor-Size Laser-Fusion Targets, Phys. Rev. Lett., 47(16):1137–1140, 1981, doi:10.1103/PhysRevLett.47.1137.
- [23] S. P. Obenschain, C. J. Pawley, A. N. Mostovych *et al.*, Reduction of Raman Scattering in a Plasma to Convective Levels Using Induced Spatial Incoherence, Phys. Rev. Lett., **62**(7):768–771, 1989, doi:10.1103/PhysRevLett.62.768.
- [24] B. E. A. Saleh and M. C. Teich, Fundamentals of Photonics, John Wiley & Sons, Inc., second edition, 2013.
- [25] Y. Gao, Y. Cui, L. Ji *et al.*, Development of low-coherence high-power laser drivers for inertial confinement fusion, Matter Radiat. Extremes, **5**, 2020, doi: 10.1063/5.0009319.
- [26] C. Dorrer, Optical parametric amplification of spectrally incoherent pulses, J. Opt. Soc. Am. B, **38**(3):792–804, 2021, doi:10.1364/JOSAB.413647.
- [27] R. K. Follet, J. G. Shaw, J. F. Myatt *et al.*, Thresholds of absolute instabilities driven by a broadband laser, Phys. Plasmas, **26**, 2019, doi:10.1063/1.5098479.
- [28] C. Dorrer, M. Spilatro, S. Herman *et al.*, Broadband sum-frequency generation of spectrally incoherent pulses, Opt. Express, **29**(11):16135–16152, 2021, doi: 10.1364/OE.424167.
- [29] R. Short and S. Skupsky, Frequency conversion of broad-bandwidth laser light, IEEE J. Quantum Electron., **26**(3):580–588, 1990, doi:10.1109/3.52136.
- [30] G. Szabó and Z. Bor, Frequency Conversion of Ultrashort Pulses, Appl. Phys. B, 58:237–241, 1994, doi:10.1007/BF01081315.
- [31] J. A. Armstrong, N. Bloembergen, J. Ducuing *et al.*, Interactions between Light Waves in a Nonlinear Dielectric, Phys. Rev., **127**(6):1918–1939, 1962, doi: 10.1103/PhysRev.127.1918.
- [32] A. V. Smith, Crystal Nonlinear Optics: with SNLO examples, AS-Photonics, 2018.
- [33] R. L. Sutherland, Handbook of Nonlinear Optics, CRC Press, 2003.
- [34] R. W. Boyd, Nonlinear Optics, Academic Press, 2003.

- [35] J. E. Midwinter and J. Warner, The effects of phase matching method and of uniaxial crystal symmetry on the polar distribution of second-order non-linear optical polarization, Brit. J. Appl. Phys., **16**:1135–1142, 1965, doi:10.1088/0508-3443/16/8/312.
- [36] V. Dmitiriev, G. Gurzadyan and D. Nikogosyan, Handbook of Nonlinear Optical Crystals, Springer, 1999.
- [37] V. Lozhkarev, G. Freidman, V. Ginzburg *et al.*, Study of broadband optical parametric chirped pulse amplification in a DKDP crystal pumped by the second harmonic of a Nd:YLF laser, Laser Phys., **15**(9):1319–1333, 2005.
- [38] D. A. Roberts, Simplified Characterization of Uniaxial and Biaxial Nonlinear Optical Crystals: A Plea for Standardization of Nomenclature and Conventions, IEEE J. Quantum Electron., **28**(10):2057–2074, 1992, doi:10.1109/3.159516.
- [39] P. C. Magnante and W. F. Hagen, Efficient Second-Harmonic Generation with Diffraction-Limited and High-Spectral-Radiance Nd-Glass Lasers, J. Appl. Phys., **40**(1):219–224, 1969, doi:10.1063/1.1657034.
- [40] C. G. Bethea and B. F. Levine, Nonlinear Susceptibility of GaP; Relative Measurement and Use of Measured Values to Determine a Better Absolute Value, Appl. Phys. Lett., **20**(8):272–275, 1972, doi:10.1063/1.1654145.
- [41] M. M. Choy and R. L. Byer, Accurate second-order susceptibility measurements of visible and infrared nonlinear crystals, Phys. Rev. B, **14**(4):1693–1706, 1976, doi:10.1103/PhysRevB.14.1693.
- [42] D. N. Nikogosyan, Nonlinear optics crystals (review and summary of data), Sov. J. Quantum Electron., 7(1):1–12, 1977, doi:10.1070/QE1977v007n01ABEH008388.
- [43] D. Eimerl, Electro-optic, linear, and nonlinear optical properties of KDP and its isomorphs, Ferroelectrics, **72**(1):95–139, 1987, doi:10.1080/00150198708017942.
- [44] R. C. Eckardt, H. Masuda, Y. X. Fan *et al.*, Absolute and Relative Nonlinear Optical Coefficients of KDP, KD*P, BaB₂O₄, LiIO₃, MgO:LiNbO₃, and KTP Measured by Phase-Matched Second-Harmonic Generation, IEEE J. Quantum Electron., **26**(5):922–933, 1990, doi:10.1109/3.55534.
- [45] S. Kielich, Optical harmonic generation and laser light frequency mixing processes in nonlinear media, Opto-electronics, **2**(3):125–151, 1970, doi:10.1007/BF01415090.

- [46] R. C. Miller, D. A. Kleinman and A. Savage, Quantitative Studies of Optical Harmonic Generation in CdS, BaTiO₃, and KH₂PO₄ Type Crystals, Phys. Rev. Lett., **11**(4):146–149, 1963, doi:10.1103/PhysRevLett.11.146.
- [47] A. V. Smith, SNLO nonlinear optics code, AS-Photonics, 2021.
- [48] A. V. Smith and R. J. Gehr, Separated-beam nonphase-matched second-harmonic method of characterizing nonlinear optical crystals, J. Opt. Soc. Am. B, **15**(8):2298–2307, 1998, doi:10.1364/JOSAB.15.002298.
- [49] A. V. Smith and W. J. Alford, Wavelength variation of the second-order nonlinear coefficients of KNbO₃, KtiOPO₄, KtiOAsO₄, LiNbO₃, LiIO₃, β -BaB₂O₄, KH₂PO₄, and LiB₃O₅ crystals: a test of Miller wavelength scaling, J. Opt. Soc. Am. B, **18**(4):524–533, 2001, doi:10.1364/JOSAB.18.000524.
- [50] L. E. Nelson, S. B. Fleischer, G. Lenz *et al.*, Efficient frequency doubling of a femtosecond fiber laser, Optics Letters, **21**:1759, 1996, doi:10.1364/OL.21.001759.
- [51] S. Lin, B. Wu, F. Xie *et al.*, Phase-matching retracing behavior: New features in LiB3O5, Applied Physics Letters, **59**:1541, 1991, doi:10.1063/1.106276.
- [52] W. Sellmeier, Zur Erklärung der abnormen Farbenfolge im Spectrum einiger Substanzen, Annalen der Physik, **219**(6):272–282, 1871, doi: 10.1002/andp.18712190612.
- [53] K. W. Kirby and L. G. DeShazer, Refractive indices of 14 nonlinear crystals isomorphic to KH2PO4, J. Opt. Soc. Am. B, 4(7):1072–1078, 1987, doi: 10.1364/JOSAB.4.001072.
- [54] G. C. Ghosh and G. C. Bhar, Temperature dispersion in ADP, KDP, and KD*P for nonlinear devices, IEEE J. Quantum Electron., **18**(2):143–145, 1982, doi: 10.1109/JQE.1982.1071501.
- [55] L. Ji, X. Zhao, D. Liu *et al.*, High-efficiency second-harmonic generation of low-temporal-coherent light pulse, Opt. Lett., **44**(17):4359–4362, 2019, doi: 10.1364/OL.44.004359.
- [56] Z. Xuezhi, W. Zhixin, W. Zhengping *et al.*, High-efficiency broadband second-harmonic-generation of YCa₄O(BO₃)₃ crystal, Applied Physics Express, **15**(5):052001, 2022, doi:10.35848/1882-0786/ac6199.
- [57] W. Demtröder, Experimentalphysik 2, Springer Verlag GmbH, 2017.

- [58] L. Mandel and E. Wolf, Coherence Properties of Optical Fields, Rev. Mod. Phys., **37**:231–287, 1965, doi:10.1103/RevModPhys.37.231.
- [59] J. M. Sousa, M. Melo, L. A. Ferreira *et al.*, Product design issues relating to rareearth doped fiber ring lasers and superfluorescence sources, **6102**:610223, 2006, doi:10.1117/12.647843, URL https://doi.org/10.1117/12.647843.
- [60] Z. Y. Zhang, R. A. Hogg, P. Jin *et al.*, High-Power Quantum-Dot Superluminescent LED With Broadband Drive Current Insensitive Emission Spectra Using a Tapered Active Region, IEEE Photonics Technology Letters, **20**(10):782–784, 2008, doi: 10.1109/LPT.2008.921108.
- [61] C. Dorrer, E. M. Hill and J. D. Zuegel, High-energy parametric amplification of spectrally incoherent broadband pulses, Opt. Express, **28**(1):451–471, 2020, doi: 10.1364/OE.28.000451.
- [62] X. Zhao, L. Ji, Y. Liu, Dong; Gao *et al.*, Second-harmonic generation of temporally low-coherence light, APL Photonics, 5:091301, 2020, doi:10.1063/5.0022307.
- [63] E. M. Campbell, T. C. Sangster, V. N. Goncharov *et al.*, Direct-drive laser fusion: status, plans and future, Philosophical Transactions of the Royal Society A: Mathematical, Physical and Engineering Sciences, **379**(2189):20200011, 2021, doi: 10.1098/rsta.2020.0011.
- [64] Y. Gao, L. Ji, X. Zhao *et al.*, High-power, low-coherence laser driver facility, Opt. Lett., **45**(24):6839–6842, 2020, doi:10.1364/OL.412197.
- [65] Gentec Electro-Optics, Inc., Datasheet Gentec QE50SP-H-MT-D0, 2020.
- [66] Gentec Electro-Optics, Inc., Datasheet Gentec QE25LP-S-MB-D0, 2020.
- [67] Gentec Electro-Optics, Inc., Datasheet Gentec S-Link, 2020.
- [68] Gentec Electro-Optics, Inc., Datasheet Gentec SOLO 2, 2020.
- [69] V. Bagnoud, B. Aurand, A. Blazevic *et al.*, Commissioning and early experiments of the PHELIX facility, Appl. Phys. B, 100:137–150, 2010, doi:10.1007/s00340-009-3855-7.
- [70] J. B. Ohland, Design and Setup of a Post-Compressor Adaptive Optics Loop at PHELIX, Ph.D. thesis, Technische Universität Darmstadt, Darmstadt, 2022, doi: 10.26083/tuprints-00021995.

- [71] E. T. Whittaker and G. N. Watson, A course of modern analysis: an introduction to the general theory of infinite processes and of analytical functions, Cambridge University Press, fourth edition, 1978.
- [72] K. E. Atkinson, An Introduction to Numerical Analysis, John Wiley & Sons, Inc., second edition, 1989.
- [73] X. Cai, X. Lin, G. Li *et al.*, Rapid growth and properties of large-aperture 98%-deuterated DKDP crystals, High Power Laser Sci. Eng., 7, 2019, doi: 10.1017/hpl.2019.24.
- [74] Z. Xuezhi, W. Zhengping, W. Xinle *et al.*, Broadband second-harmonic-generation in GdCOB crystals, Opt. Express, **30**(5):6546–6555, 2022, doi:10.1364/OE.451703.
- [75] H. Zhu, T. Wang, W. Zheng *et al.*, Efficient second harmonic generation of femtosecond laser at 1 μm, Optics Express, **12**:2150, 2004, doi:10.1364/OPEX.12.002150.
- [76] M. S. Webb, D. Eimerl and S. P. Velsko, Wavelength insensitive phase-matched second-harmonic generation in partially deuterated KDP, Journal of the Optical Society of America B, 9:1118, 1992, doi:10.1364/JOSAB.9.001118.
- [77] A. Yokotani, T. Sasaki, K. Yoshida *et al.*, Extremely high damage threshold of a new nonlinear crystal L-arginine phosphate and its deuterium compound, Applied Physics Letters, **55**(26):2692–2693, 1989, doi:10.1063/1.101969.